National Aeronautics and Space Administration

Titan Geomorphological Units with Cassini/VIMS and SAR

Principal Investigator: Anezina Solomonidou (3220)

R.M.C. Lopes (3220); **A. Coustenis** (Observatory of Paris, FR); **S. Rodriguez** (AIM Laboratory, FR); **M. Malaska** (3227); **C. Sotin** (4000); **K. Lawrence** (4000); **M. Janssen** (1191); **R.H. Brown** (University of Arizona, USA)

Introduction — Titan, Saturn's largest satellite, has a **complex atmosphere and surface**, making it a key area for planetary research

Goal — Key factor for Titan's geologic evolution: **constrain the composition** of the different geomorphologic units

Problem — VIMS: The extended, dense and hazy atmosphere due to **methane** (1.5% in the stratosphere and 5% at the surface)

Our approach — We utilize **several Cassini datasets** processed in novel ways. Absolute surface albedo at all methane windows with **new methane coefficients** using a **Radiative transfer code** + morphology + composition
= **new and enhanced science**

Innovation — First Titan study to use the most complete to date and updated radiative transfer code in addition to the simultaneous use of RADAR data

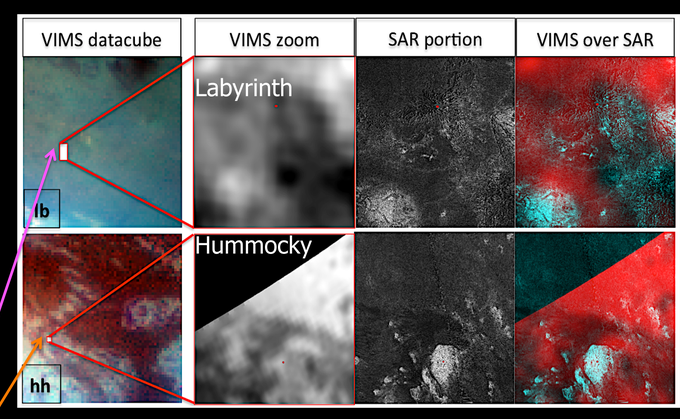

Data & Method

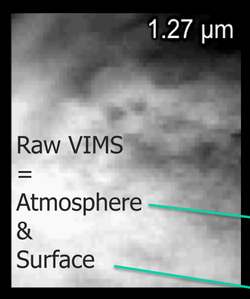

'Methane windows' centered at 0.93, 1.08, 1.27, 1.59, 2.03, 2.69-2.79 and 5.00 μm

↓

Use of theoretical and experimental data in a modular Radiative Transfer model

↓

Haze effect
+
Surface albedo

Solomonidou et al. (2014; 2016)

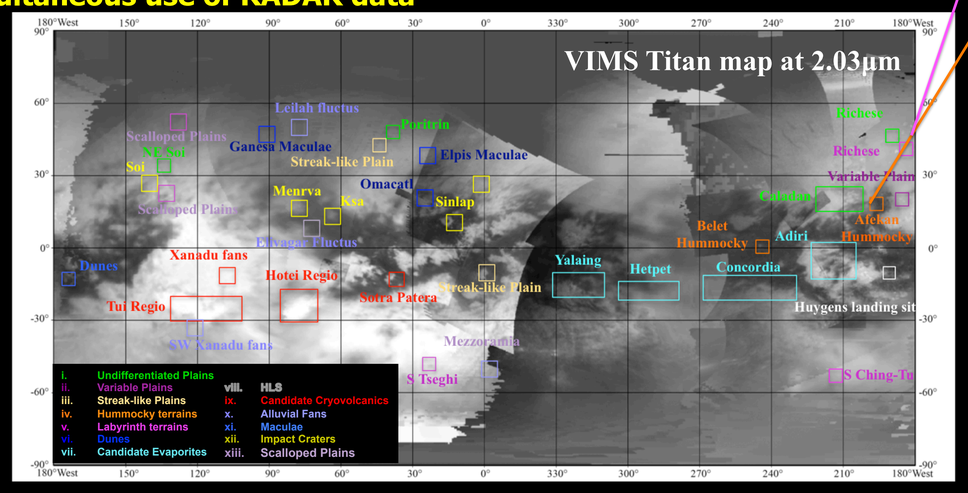

Significance

- ✓ Promising landing sites
- ✓ Future mission enhancements
- ✓ Habitability

Geologically active areas could be utilized as future mission landing sites

Surface albedos vs Titan constituents

Interpretations

Absolute surface albedo maps

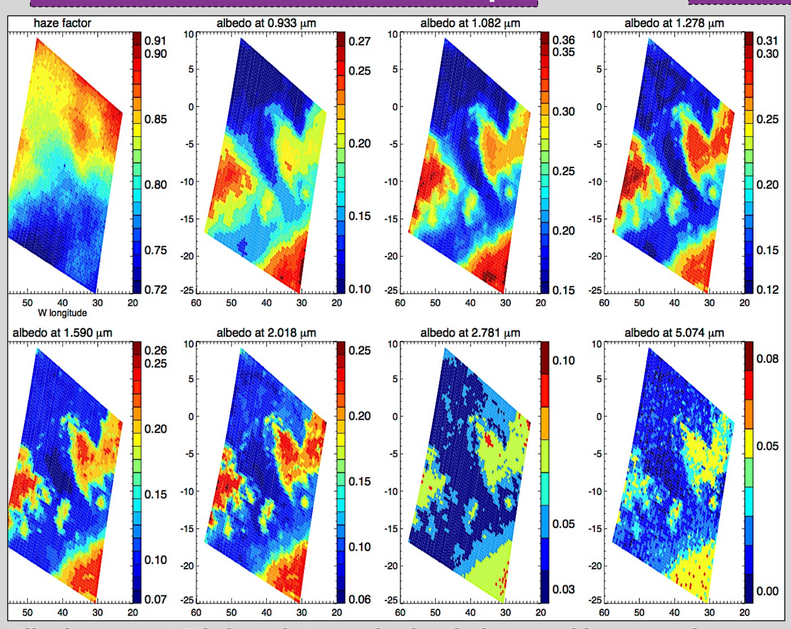

Albedo maps at 7 infrared atmospheric windows and haze opacity.
Example of simultaneous extraction of haze opacity and surface albedo.
The inversion of the entire datacube (64x64 spectra) took less than 1 minute.

Albedo + SAR

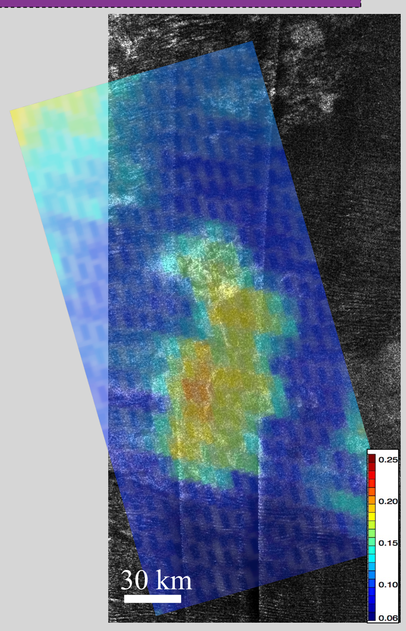

Sotra Patera region
Albedo + morphology

Absolute surface albedo

vs

Titan candidate constituents

CH_4, C_2H_2, C_2H4, C_2H_6, C_3H_8, CO_2, NH_3, H_2O, HC_3N, tholin, bitumen, amorphous carbon

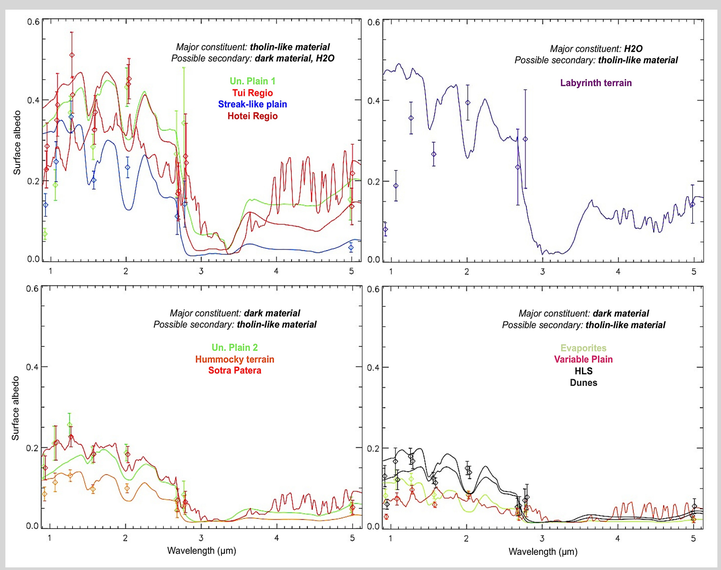

Haze contribution to VIMS spectra =
from -30% to +10% of the "nominal" DISR value valid at the HLS.

Major constituent	Secondary	Geomorphological Unit
Tholin-like		
	H_2O	Streak-like plains
	H_2O	Hotei Regio
	Dark material	Undifferentiated plains 1
	Dark material	Tui Regio
H_2O		
	Tholin-like	Labyrinth terrain
Dark material		
	Tholin-like	Hummocky terrain
	Tholin-like	Variable plains
	Tholin-like	Evaporite candidates
	Tholin-like	HLS
	Tholin-like	Dunes
	Tholin-like	Sotra Patera
	Tholin-like	Undifferentiated plains 2

Possible secondary

- H_2O
- Dark material
- Tholin-like

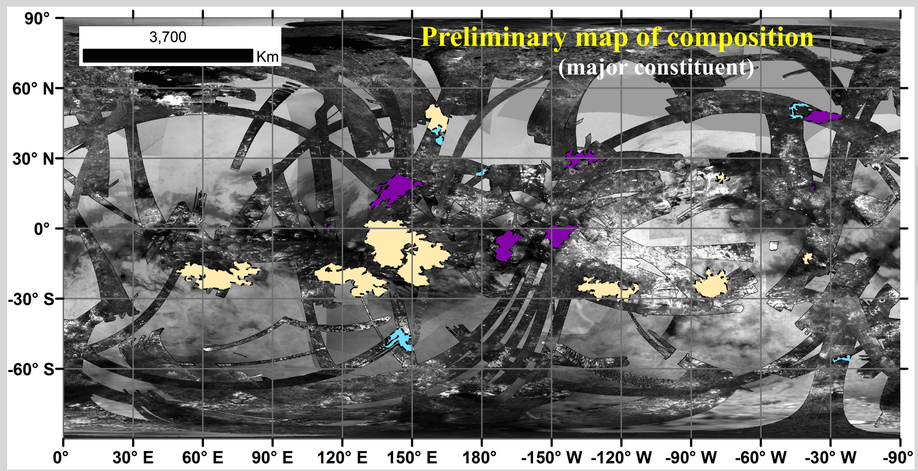

Tholin-like material
H_2O ice
Dark material

Results

- 3 major classes of surface albedo on Titan's mid-latitudes
- 3 regimes in composition: Tholin - H_2O - dark material
- 2 areas showing recent changes (Tui Regio + Sotra Patera)

NEXT STEP: CONFIGURATION OF PROCESSES

Exogenic Processes

- ✧ Evaporitic, fluvial, or lacustrine deposits
- ✧ no connection to the interior
- ✧ precipitation of methane rain and/or tholins

Endogenic Processes

- ✧ Cryovolcanic deposits
- ✧ Brightening or darkening due to resurfacing of an initially cryovolcanic terrain

Importance

-energy
-methane reservoir
-interior/surface/atmosphere exchanges
-support for life

National Aeronautics and Space Administration
Jet Propulsion Laboratory
California Institute of Technology
Pasadena, California
www.nasa.gov

Papers from this work while at JPL:
1. ***Solomonidou et al.*** *(2014)*. Surface albedo spectral properties of geologically interesting areas on Titan. JGR, 119, 1729-1747.
2. *Sohl,* ***Solomonidou et al.*** *(2014).* Structural and tidal models of Titan and inferences on cryovolcanism. JGR, 119, 1013-1036.
3. ***Solomonidou et al.*** *(2016).* Temporal variations of Titan's surface with Cassini/VIMS. Icarus, 270, 85-99.
4. *Lopes,* ***Solomonidou et al.*** *(*2016). Nature, Distribution, and Origin of Titan's Undifferentiated Plains. Icarus, 270, 162-182
5. Bonnefoy, **Solomonidou et al.** (2016). Compositional and spatial variations in Titan …Cassini VIMS and RADAR. Icarus, 270, 222-237.
6. Sotin, **Solomonidou et al.** (2016). In preparation.

Poster No. P-1

National Aeronautics and Space Administration

UV Attenuation in Mars Analog Minerals and Implications for the SHERLOC Mars 2020 Instrument

Author: Brandi Carrier (3220)
Luther Beegle (3200), Rohit Bhartia (3225), William Abbey (3225)

Introduction

The SHERLOC Mars 2020 Instrument utilizes a Deep UV laser (248.6 nm) to induce Raman and fluorescence in organics and minerals. SHERLOC will use these abilities on Mars to identify, in situ, interesting samples for sample caching and potential subsequent return to Earth. The attenuation rate of UV photons in martian mineral substrates will determine the depth to which various organics can be detected. The penetration depth of UV radiation also has implications for habitability and biosignature preservation.

Here we report on results obtained using a SHERLOC-like laser to detect organics under thin layers of 4 different minerals – Gypsum, Bishop Tuff, Kaolinite and MMS Basalt. A separate study has been conducted to determine UV attenuation rates as a function of depth for these Mars analog minerals. These results will be used to constrain detection limits for the SHERLOC instrument as well for future investigations into subsurface UV photolysis of organic molecules.

Methods

Bulk Attenuation of UV Radiation

- Mineral Substrates:
  - Basalt (MMS-Mojave Mars Simulant)
  - Gypsum
  - Kaolinite
  - Bishop Tuff
- 1000 W Xe Arc Lamp
- Spectrometer
  - 0.4 nm resolution
  - Radiometrically calibrated

Subsurface Detection of Organics

- Laser Information:
  - 248.6 nm
  - 40 Hz
  - Fluorescence 25 pulses per point
  - Raman 1200 pulses per point
- Organics
  - Phenylalanine
  - Alanine
  - Phenanthrene
  - Histidine
- 156 Spectra per sample
- Top Mineral Layer: ~100-200 µm

Results

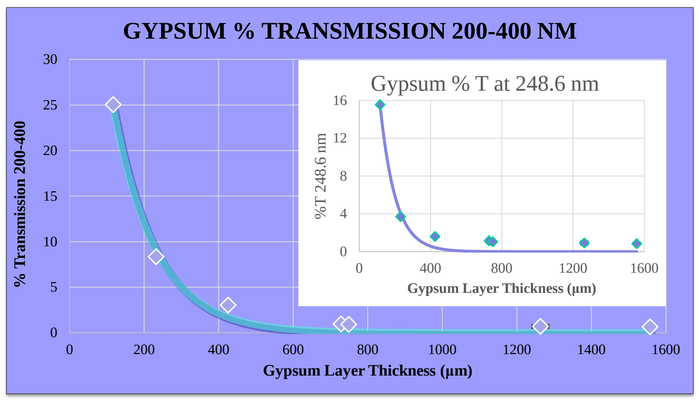

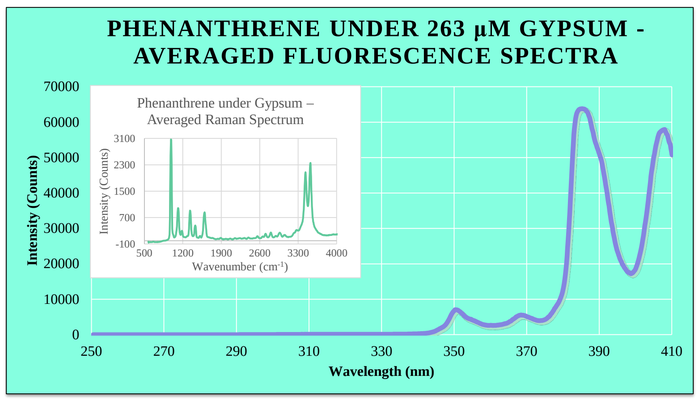

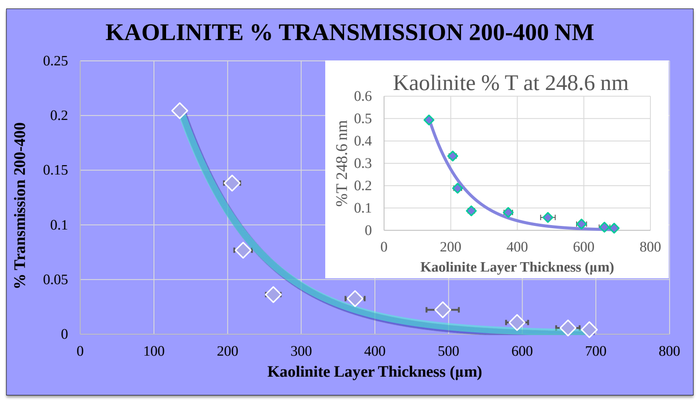

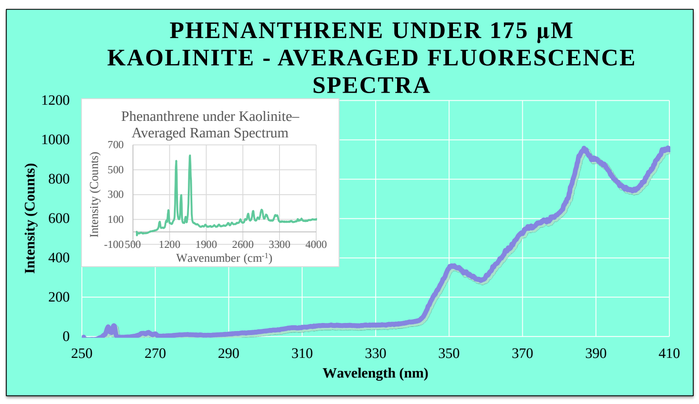

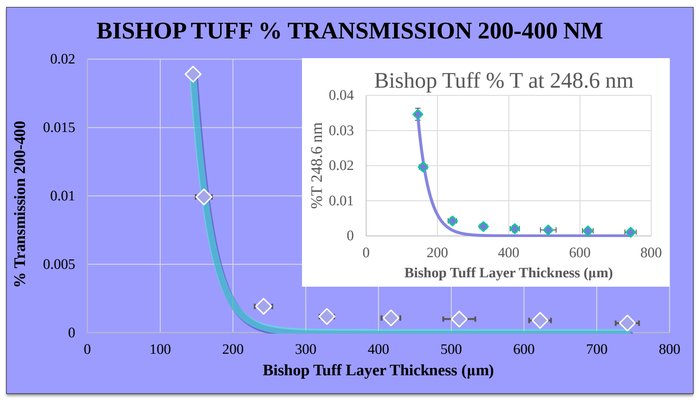

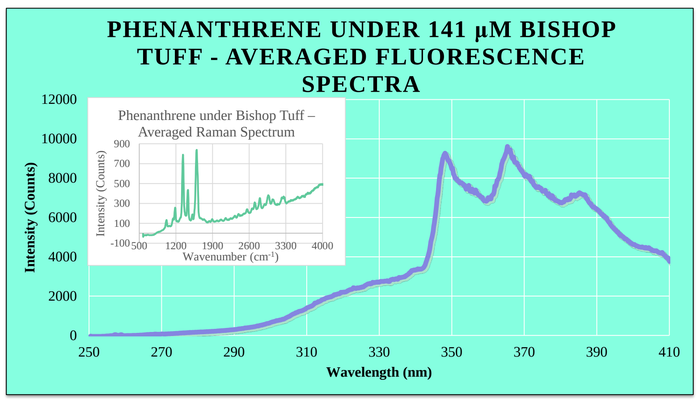

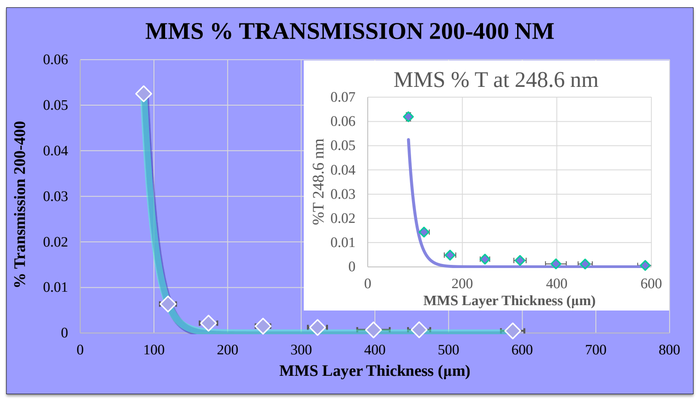

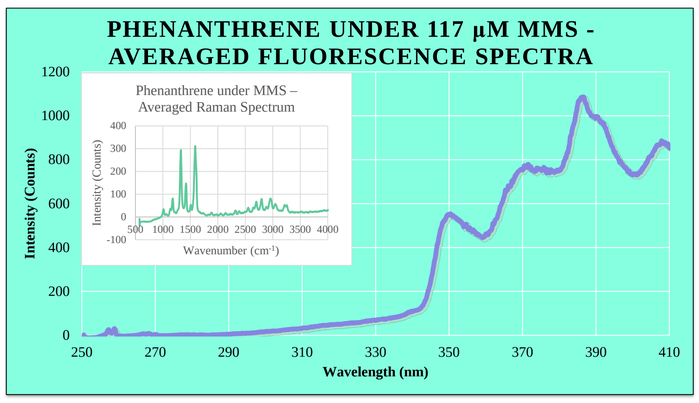

Conclusions

- Aromatic organics such as phenanthrene can be detected to depths >200 µm
- Aliphatic organics such as alanine can be detected to depths >100 µm
- UV Transmission is greatest in Gypsum>Kaolinite>Bishop Tuff>MMS Basalt
- Variability in transmission from point to point due to heterogeneity in the mineral matrix
- Transmission is dependent on wavelength
- Organics in the near sub-surface are likely modified by solar UV radiation

Future Work

- Investigate greater variety of minerals and organics
- Determine absolute limit of detection depth for SHERLOC
- Determine effects of solar UV on organic survival in the near sub-surface

National Aeronautics and Space Administration
Jet Propulsion Laboratory
California Institute of Technology
Pasadena, California
www.nasa.gov

National Aeronautics and Space Administration
Jet Propulsion Laboratory
California Institute of Technology
Pasadena, California

www.nasa.gov

National Aeronautics and Space Administration

Characterising Jupiter's stratosphere-auroral interactions during the Juno mission

James Sinclair[a]

Glenn S. Orton[a], Thomas K. Greathouse[b], Julie Moses[c], Vincent Hue[b], Leigh N. Fletcher[d], Patrick G. J. Irwin[e], Henrik Melin[d], Rohini Giles[e]

[a]Division 3222, Jet Propulsion Laboratory/Caltech [b]Southwest Research Institute [c]Space Science Institute [d]University of Leicester [e]University of Oxford

P-3

Jupiter's auroral-related mid-infrared emission

- Charged particles of the solar wind and of the Galilean satellites' (Io, Europa, Ganymede) tori penetrate Jupiter's atmosphere at polar latitudes.
- Ion/electron precipitation yields aurora emission at ultraviolet (Figure 1a) and near-infrared (H_3^+ emission, Figure 1b) wavelengths.
- Mid-infrared CH_4 emission also enhanced in auroral regions (Figure 1c), which indicates elevated stratospheric temperatures.
- Thus, auroral energy reaches Jupiter's stratosphere and modifies the thermal structure and composition. However, this mechanism is still not well understood.

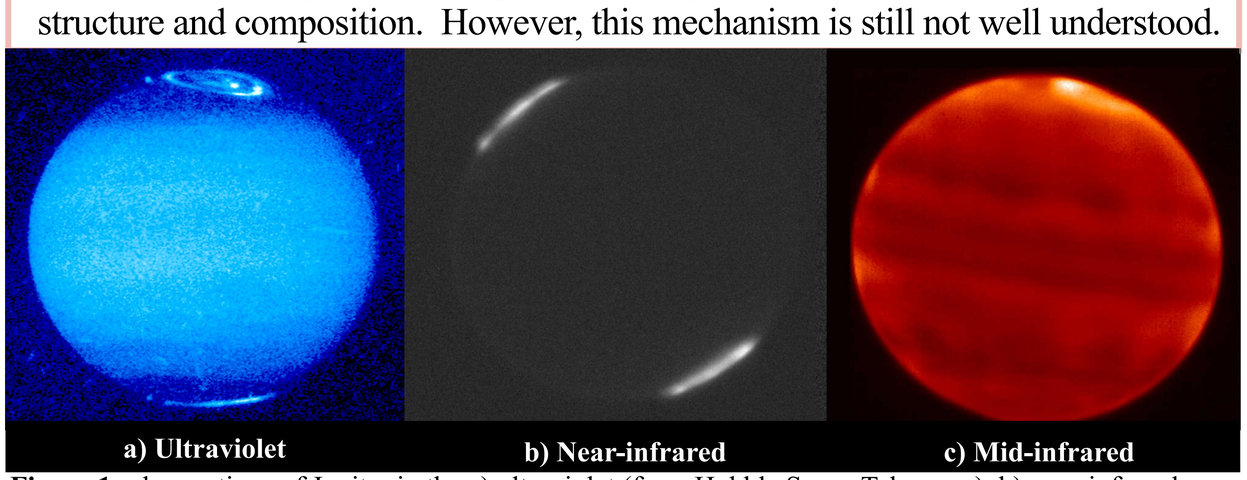

Figure 1: observations of Jupiter in the a) ultraviolet (from Hubble Space Telescope), b) near-infrared (SpeX on NASA's Infrared Telescope Facility) and c) mid-infrared (COMICS on Subaru).

The Juno mission

- Juno arrived in orbit around Jupiter in July 2016 and its science payload becomes operational in November 2016.
- Auroral processes in Jupiter's ionosphere can be studied in the ultraviolet and near-infrared by Juno's Ultraviolet Spectrometer (UVS) and Jovian Infrared Auroral Mapper (JIRAM) respectively.
- However, Juno has no mid-infrared instrument (5 - 15 um) capable of studying auroral effects on the stratosphere.
- Ground-based mid-infrared observations are required to characterise stratospheric auroral effects.

Project Goals

1) Provide ground-based mid-infrared monitoring of auroral effects on Jupiter's stratosphere using the TEXES instrument on NASA's Infrared Telescope Facility (IRTF).
2) Aim to better understand the mechanisms for auroral forcing of the stratosphere by studying its temporal evolution at a time when Juno is measuring the external magnetospheric environment.
3) Determine stratospheric temperature/composition information to enhance the scientific return of Juno's UVS and JIRAM instruments.

Ground-based mid-infrared support from IRTF-TEXES

- The **T**exas **E**chelon **C**ross **E**chelle **S**pectrograph on NASA's **I**nfra**r**ed **T**elescope **F**acility (3m telescope at Mauna Kea, HI).
- TEXES can measure spectra at very high spectral resolutions (R = 20000 - 85000), which sounds the jovian stratosphere over a much larger altitude range (10 - 0.001 mbar) compared to Cassini-CIRS (Figure 2).
- This is particularly ideal for resolving the high altitudes at which auroral energy is deposited.

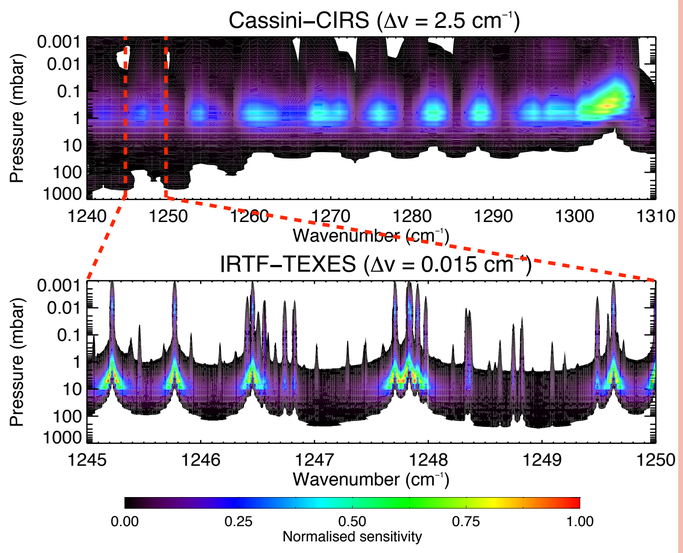

Figure 2: The normalised sensitivity to temperature as a function of pressure and wavenumber for Cassini-CIRS (top) and IRTF-TEXES (bottom).

Temperature retrieval method

- Retrievals were performed using NEMESIS (Irwin et al., 2008, JQSRT 109:1136-1150), an inverse radiative transfer code.
- The vertical temperature profile was retrieved by fitting the H_2 S(1) and CH_4 emission features and iterating towards a solution that optimised the fit to the spectra - Figure 3.

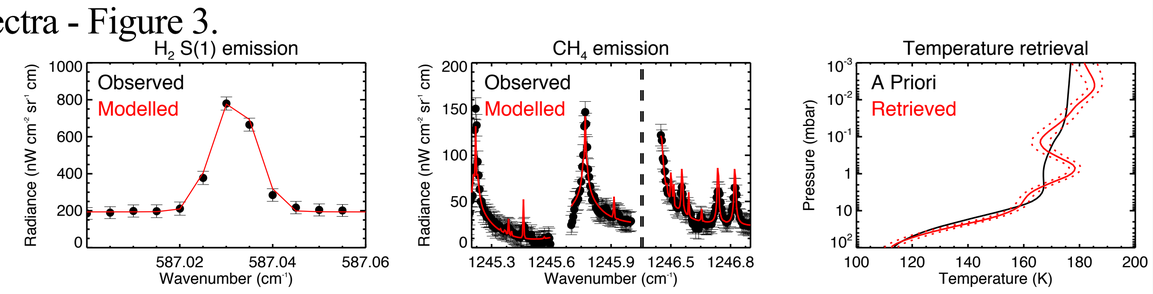

Figure 3: Observed (points with error bars) and modelled (red) spectra of H_2 S(1) (left) and CH_4 (middle) emission and the corresponding retrieved temperature profile (right).

Temperature results from 2014 and 2016

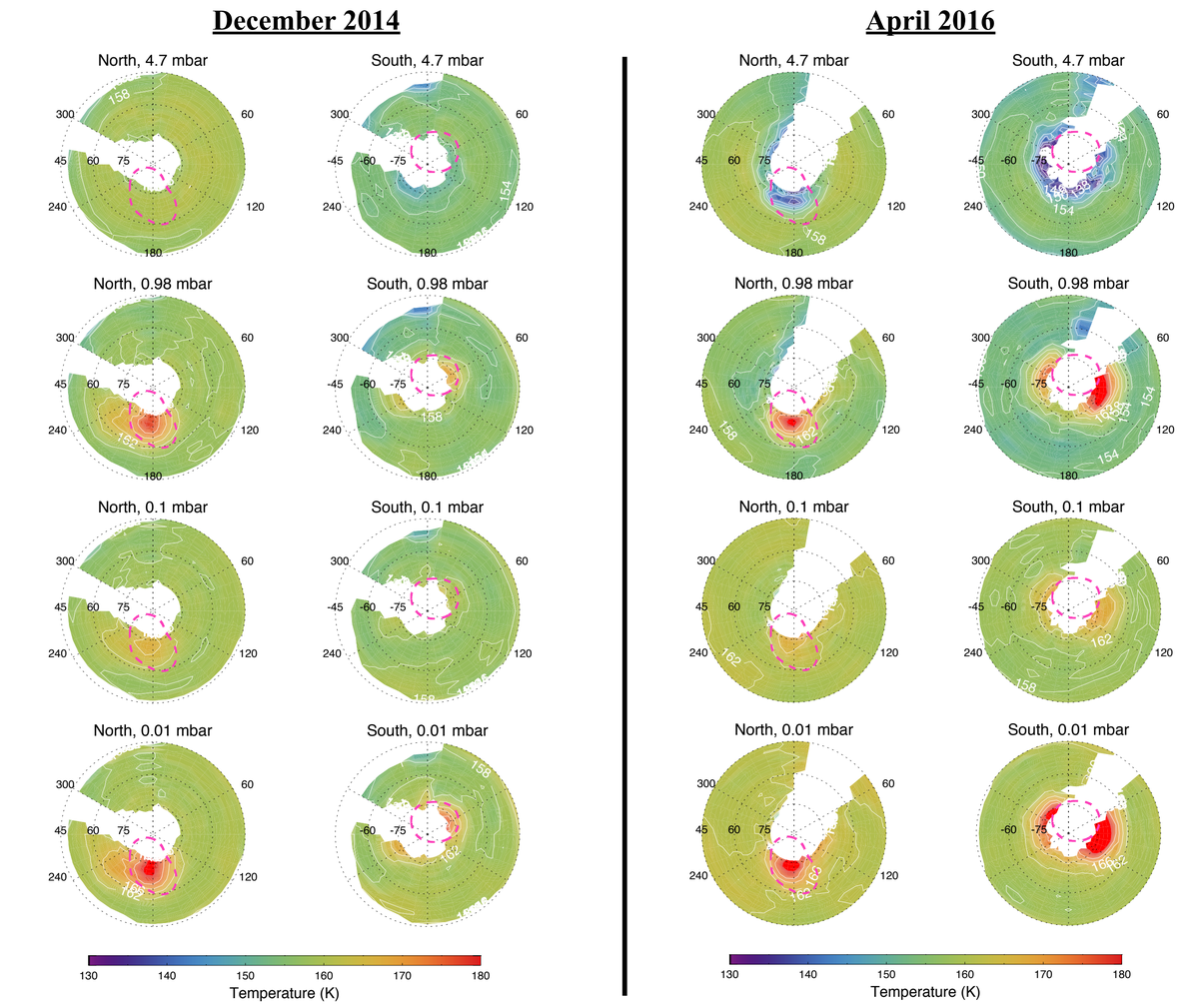

Figure 4: Retrievals of temperature from IRTF-TEXES spectra in 2014 (left) and 2016 (right) at 4.7 mbar (top row), 0.98 mbar (2nd row), 0.1 mbar (3rd row) and 0.01 mbar (bottom row). The dashed red lines mark the positions of the auroral ovals as seen in the ultraviolet (Bonfond et al., 2012, GRL 39:L01105).

Conclusions

- No evidence of auroral heating at pressures higher than 1 mbar.
- Auroral heating evident at two discrete pressure levels - 1 mbar and 0.01 mbar - with little heating at intermediate pressures.
- Heating at 1 mbar level believed to result from production of aerosols and their absorption of shortwave radiation, while heating at pressures of 0.01 mbar and lower believed to result from joule heating and ion/electron precipitation.
- The magnitude and position of the northern auroral hotspot remains fixed from 2014 to 2016. Southern auroral-heating has increased dramatically from 2014 to 2016 and the orientation of the hotspot has moved westward.

Future Work

- Use awarded IRTF-TEXES telescope time in December 2016 and January 2017 to obtain similar maps of temperature during Juno's 5th and 9th orbits.
- Propose further IRTF-TEXES time in 2017/2018 to increase temporal coverage and support Juno's later orbits.

Thermally induced stresses in boulders on the Moon: Implications for breakdown

Jamie Molaro

Jet Propulsion Laboratory, California Institute of Technology; Correspondence: jmolaro@jpl.nasa.gov

National Aeronautics and Space Administration

Poster # P - 4

Background

The expansion and contraction of rocks undergoing diurnal thermal cycling contributes to microcrack propagation and rock breakdown over time. The amount of stress induced during a thermal cycle is directly proportional to the diurnal temperature range. This suggests that airless bodies, as wells as bodies with long solar days and/or small solar distances, are most susceptible to this process. Research suggests it may be active on (among others) the Moon, Mercury, and near-Earth asteroids (e.g. 3200 Phaethon), contributing to the degredation of craters and ejecta and the production of regolith on these surfaces. However, the nature and extent of the damage is not well constrained. Understanding the role this process plays in the evolution of these surfaces has important implications for quantifying crater ages, regolith depth, boulder size-frequency distributions, and surface characteristics on these bodies. Here we model the thermomechanical behavior of boulders of varying size on the surface of the Moon, and investigate the magnitude and distribution of stresses induced by diurnal thermal forcing.

Model

Models were completed using the 3D finite element modeling software **COMSOL Multiphysics**. The geometry consists of a spherical boulder of varying diameter embedded halfway in a volume of regolith. Using COMSOL, **we imposed solar radiation on the gemoetry by defining the sun as a point source with a time-dependent position in the sky for an equatorial lunar surface.** The effects of local slope and aspect angle, size of the solar disc, and scattered radiation between the regolith and rock surfaces are accounted for at each point on the geometry surface. The heat and displacement equations are then calculated over one solar day.

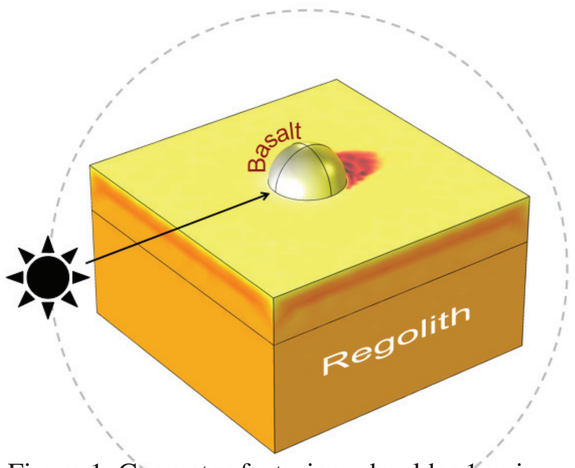

Figure 1. Geometry featuring a boulder 1 m in diameter, embedded in volume of regolith 8 m wide and 4.5 m deep.

Table 1. Values for the material properties used for regolith and rock. The regolith density and thermal conductivity are temperature and depth dependent*, as is the heat capacity* for both materials.

	Rock	Regolith
Density (kg/m^3)	3150	f(z)
Thermal Conductivity (W/mK)	2	f(T,z)
Heat Capacity	f(T)	f(T)
Young's Modulus (GPa)	50	0.008
Coefficient of Thermal Expansion (1/K)	10^{-5}	10^{-4}
Poisson's Ratio	0.23	0.4
Surface Emissivity	0.95	0.98

* Vasavada et al. (2012) *Geoph. Res. Letters*, 117, E00H18.
Ledlow et al. (1992) *The Astrophys. J.*, 384, 640-655.

Results presented are the **maximum principal stress,** which represents the most amount of **tensile stress** at a given location and time. This is the conventional parameter used for brittle failure, and can be thought of as the amount of idealized energy available to propagate cracks.

Results

Temperature and Stress for a 1 m Boulder

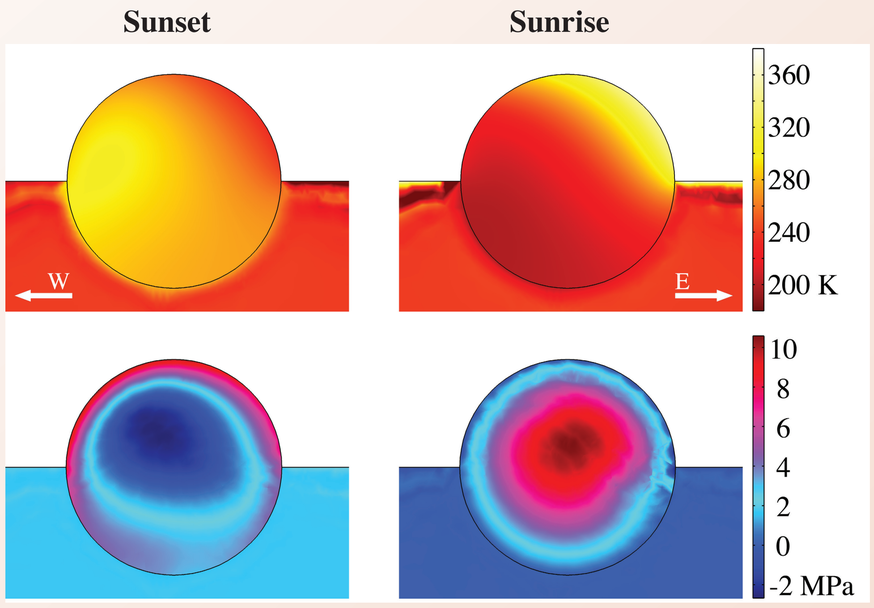

Surface cooling and contraction creates surface-parallel stresses at boulder's edge.

Induced temperature gradient during heating creates stresses at the boulder's interior.

Figure 2. Snapshots of the temperature (top) and stress (bottom) in a 2D cut plane through a 1 m diameter boulder during sunrise (right) and sunset (left). The cut plane is an E-W profile through the center of the boulder. **Peak stresses occur bimodally at these times, at the boulder's interior and surface near sunrise and sunset, respectively.** Interior stresses are associated with macroscopic temperature gradients set up during overnight cooling, whereas surface stresses occur due to cooling and contraction of the surface.

National Aeronautics and Space Administration
Jet Propulsion Laboratory
California Institute of Technology
Pasadena, California
www.nasa.gov

Peak Surface Stress with Boulder Size

Figure 3. Profiles of surface stresses in boulders with diameters from 0.3 to 1 m throughout the lunar day, taken at the location in the boulder where the maximum stress occurs. **Stresses increase with boulder size, suggesting larger boulders may break down faster.** The dashed and dotted profiles show the stress at the top and bottom edges of a 30 cm boulder buried by 2.5 cm of regolith. **This boulder responds only weakly to thermal forcing, suggesting a threshold below which thermal breakdown may not occur.** The dashed vertical lines show the times of sunrise, noon, and sunset.

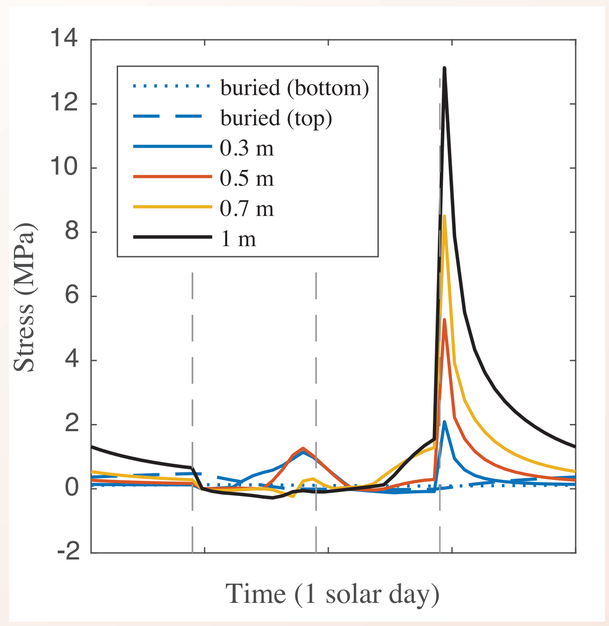

Figure 4. The surface curvature of small rocks (right) allows for the relief of stresses induced during expansion and contraction. In contrast, a very large rock acts similarly to an infinite halfspace (left), which experiences no change in surface area, and thus no stress relief.

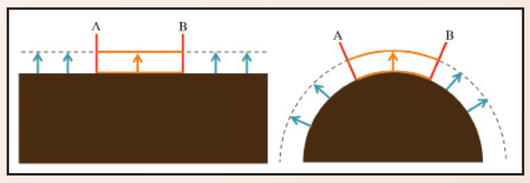

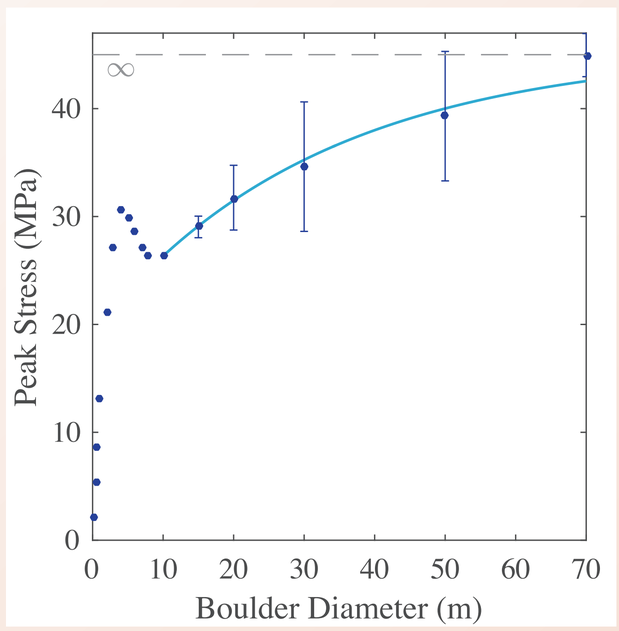

Figure 5. Peak surface stress with boulder diameter (dots), with an exponential curve fit to boulders ≥10 m, occurs in two regimes. Stresses in boulders up to ~5x the diurnal skin depth (~4 m) in diameter occur at sunset, and are controlled by the heat flux out of the boulder surface. As the thermal wave loses contact with the boulder interior (≥10 m), the heat flux decreases and surface contraction occurs continuously throughout the night, leading to peak stresses just before sunrise. Simultaneously, the behavior of an element at the boulder edge approaches that of an infinite halfspace (see Fig 4), preventing stress relief. Boulders ~4 m in size, the transition between regimes, have only moderately lower stresses than in larger (≥10 m) boulders, but much less material to erode. **This suggests that boulders ~5x the diurnal skin depth in size may be preferentially removed by this process on airless bodies.**

Stress Orientations and Crack Propagation

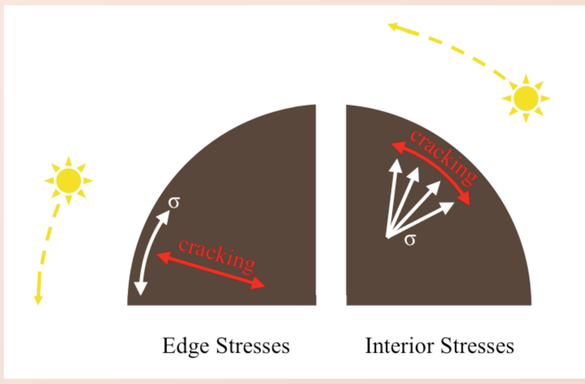

Figure 6. Stress orientations can yield insight into how breakdown may occur. Interior stresses act on a plane perpendicular to the path of the sun, driving the propagation of surface-parallel cracks and contributing to exfoliation of planar fragments. Exterior stresses act parallel to the boulder surface driving the propagation of surface-perpendicular cracks and contributing to granular disintegration. **These two mechanisms likely work together to hasten disaggregation of the near-surface.**

Conclusions

Our results show that large boulders experience higher stresses than smaller boulders, suggesting they are more susceptable to thermal breakdown and expereince faster breakdown rates. Peak stresses are bimodal, occurring at sunrise and sunset, at the boulder's interior and surface, respectively. Both of these kinds of stresses work together to disaggregate material in the near-surface. Boulders with regolith cover and those ≤30 cm in diameter likely do not experience thermal breakdown. However, the amount of stress in real boulders will be affected by complexities such as the amount of pre-existing damage and structural weaknesses, as the propagation of cracks and movement of microcrack walls will relieve stress. **This suggests that breakdown is most effective in fresh boulders from new impacts.** Better constraining breakdown rates of these boulders will have important implications for understanding crater and ejecta field ages. On Earth, the amount of stress needed to cause fatigue breakdown is on the order of 10 MPa, suggesting this process is active on the Moon. However, atmosphere plays a strong role in crack propagation processes. **More laboratory work on fatigue processes in vacuum is needed to better constrain breakdown.**

Acknowledgement: Part of this work was supported by an appointment to the NASA Postdoctoral Program at the Jet Propulsion Laboratory, California Institute of Technology, under contract with NASA, administered by the Universities Space Research Association through a contract with NASA.

National Aeronautics and Space Administration

The Surface and Interior Evolution of Ceres Revealed by Fractures and Secondary Crater Chains

Jennifer E. C. Scully (322 - Jennifer.E.Scully@jpl.nasa.gov)
Carol A. Raymond (408) & Julie C. Castillo-Rogez (322)

INTRODUCTION/PROBLEM

- In March 2015, Dawn, a JPL mission, became the first spacecraft to orbit Ceres, the largest body in the asteroid belt (~470 km radius) & only inner solar system dwarf planet
- Pre-Dawn knowledge of Ceres: at least partially differentiated, pervasive viscous relaxation & water-ice-rich outer layer (e.g. Bland, 2013; Castillo-Rogez & McCord, 2010; Drummond et al., 2014)
- Post-Dawn knowledge of Ceres: less differentiated, little viscous relaxation & outer layer of silicates, salts & water ice (e.g. Bland et al., 2016; Castillo-Rogez et al., 2016; Fu et al., 2016; Park et al., 2016)
- What do the ≥1 km wide linear features observed on Ceres' surface reveal about Ceres' surface & interior evolution?

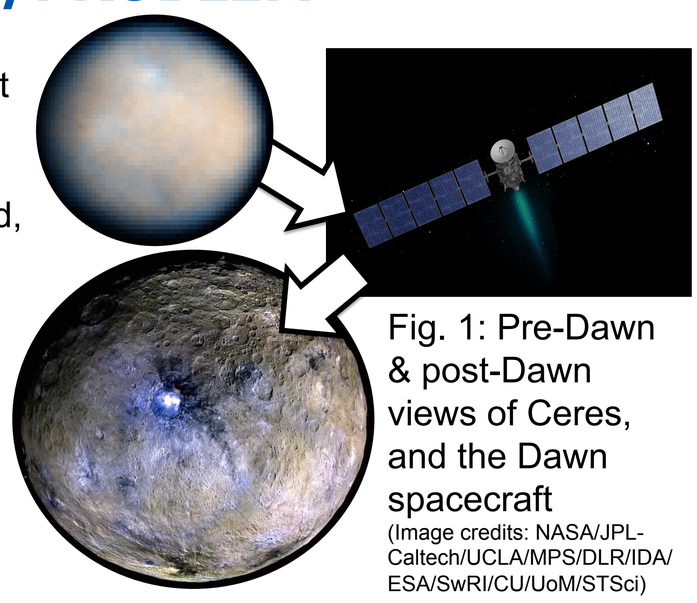

Fig. 1: Pre-Dawn & post-Dawn views of Ceres, and the Dawn spacecraft (Image credits: NASA/JPL-Caltech/UCLA/MPS/DLR/IDA/ESA/SwRI/CU/UoM/STSci)

METHODOLOGY

- Digitally map all ≥1 km wide linear features on Ceres using ESRI ArcMap 10.3 software (allows for georeferencing & use of multiple datasets)
- Mapping based on 140 m/pixel image mosaics from the Framing Camera (FC) (Roatsch et al., 2016)
- Mapping in regions of interest updated with 35 m/pixel FC image mosaics (Roatsch et al., 2016)
- Mapping also informed by shape models derived from FC data (Preusker et al., 2016; Park et al., 2016), color images from the FC color filters & spectral data from the Visible-Infrared Mapping Spectrometer (VIR) (De Sanctis et al., 2015)

RESULTS

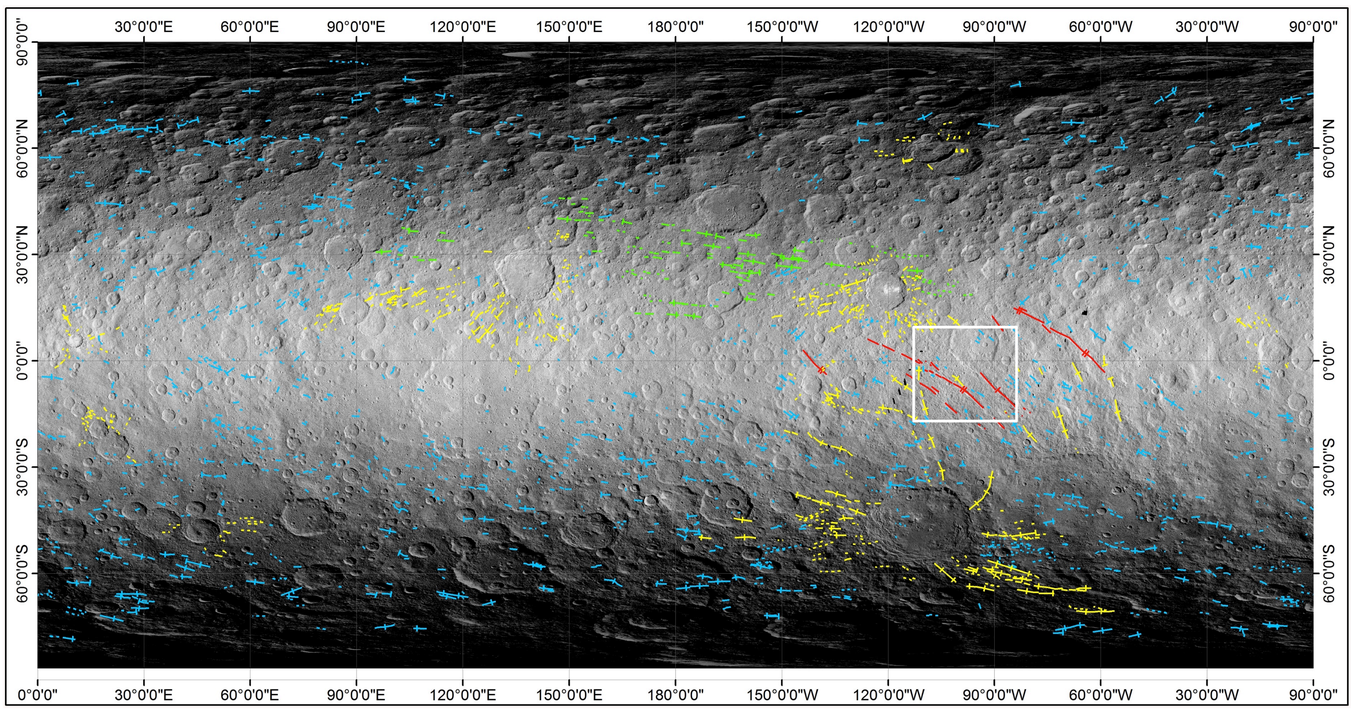

Fig. 2: Geologic map of four types of linear features (white box shows area of Fig. 3)

- We mapped four types of ≥1 km wide linear features:
  - Red: Samhain Catenae pit chains => interpreted as the surface expression of sub-surface fractures
  - Yellow: secondary crater chains => interpreted to form as material ejected during formation of an identified impact crater impacts the surface in a radial pattern around the impact crater
  - Green: Junina Catenae secondary crater chains => interpreted to form as material ejected during formation of an identified impact crater impacts the surface in a non-radial pattern far from the impact crater
  - Blue: secondary crater chains => interpreted to form as material ejected during formation of an unidentified impact crater impacts the surface
  - Note: pit chains are chains of rimless/unevenly-shaped pits
  - Note: secondary crater chains are chains of rimmed/circular bowls

INTERPRETATIONS/CONCLUSIONS

- What the linear features reveal about Ceres' surface & interior evolution:
  - The formation & preservation of linear features reveals that:

    Ceres' outer layer is relatively strong, and is not dominated by viscous relaxation as predicted
  - In combination with modeling studies (Schmedemann et al., 2016; Neesemann et al., 2016), we interpret that the Junina Catenae secondary crater chains form as material ejected during formation of an identified impact crater impacts the surface in a non-radial pattern far from the source impact crater, which reveals that:

    Ceres' fast rotation (~9 hours) & relatively small radius (~470 km) can cause secondary craters to form far from their source impact crater
  - Applying a fracture spacing to fractured layer thickness ratio of ~1 (e.g. Bai & Pollard, 2000) to the Samhain Catenae fractures tells us that:

    Ceres' outer, fractured layer is ~88 km thick
  - We interpret that the Samhain Catenae formed due to uplift and extension induced by an upwelling region, which, in combination with geodynamic modeling (King et al., 2016), indicates that:

    Plumes occurred at depth during Ceres' evolution

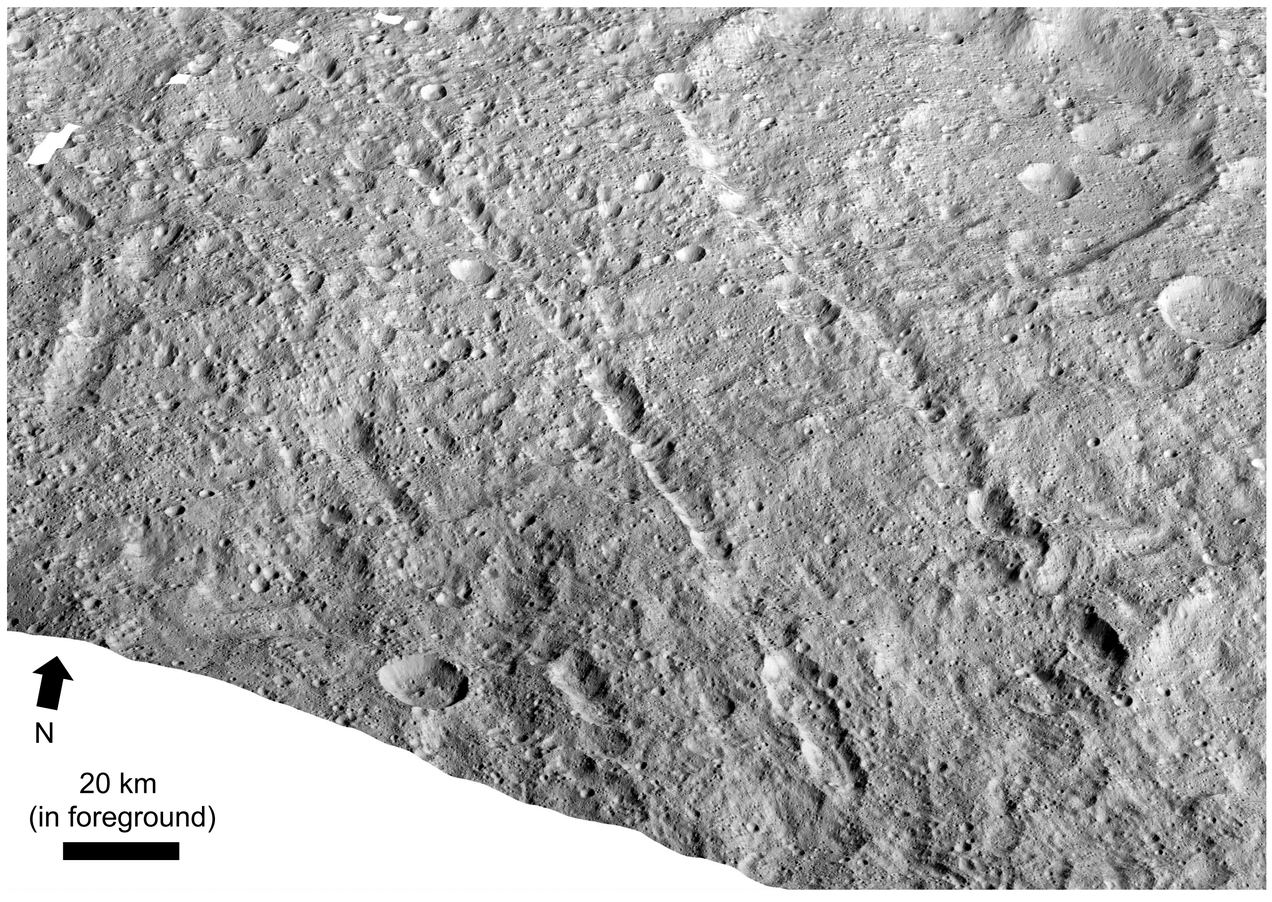

Fig. 3: Perspective view of part of the Samhain Catenae pit chains (35 m/pixel)

National Aeronautics and Space Administration
Jet Propulsion Laboratory
California Institute of Technology
Pasadena, California

www.nasa.gov

Additional co-authors:
Debra L. Buczkowski[1], Scott D. King[2], Nico Schmedemann[3], David P. O'Brien[4], Simone Marchi[5], Christopher T. Russell[6], Giuseppe Mitri[7] & Michael Bland[8].
[1]JHU-APL, Laurel, MD, USA, [2]Virginia Tech, Blacksburg, VA, USA, [3]Free University of Berlin, Berlin, Germany, [4]PSI, Tucson, AZ, USA, [5]Southwest Research Institute, Boulder, CO, USA, [6]UCLA, Los Angeles, CA, USA, [7]University of Nantes, Nantes, France, [8]USGS Astrogeology Science Center, Flagstaff, AZ, USA.

Acknowledgements:
We thank the Dawn Flight Team at JPL for the development, cruise, orbital insertion and operations of the Dawn spacecraft at Ceres. We thank the instrument teams at the Max Planck Institute, German Aerospace Center (DLR), Italian National Institute for Astrophysics (INAF) and Planetary Science Institute (PSI) for the acquisition and processing of Dawn data.

Poster No. P-5

National Aeronautics and Space Administration

A New Method for Mapping the Rock Size Frequency Distribution on the Moon using Diviner Infrared Measurements

C. Elder[1] (3223), P. Hayne[1] (3223), S. Piqueux[1] (3222), J. Bandfield[2], J.-P. Williams[3], R. Ghent[4], D. Paige[3]

[1]Jet Propulsion Laboratory, California Institute of Technology, [2]Space Science Institute, [3]University of California Los Angeles, [4]University of Toronto

Synopsis

- Nighttime multispectral measurements by the Lunar Reconnaissance Orbiter (LRO) Diviner Radiometer and 3D thermal models of rocks are used to map the lunar rock size frequency distribution.
- Motivation:
  - Characterizing the lunar rock distribution is necessary for selecting safe landing sites and for planning sample acquisition for future lander and rover missions.
  - Different rock size frequency distributions indicate different geologic processes and ages.
  - High-resolution imagery only covers small regions. Diviner has obtained global coverage of the Moon.
  - Previous work using thermal infrared data to derive rock abundance was only sensitive to rocks larger than 1 m [e.g. 1].
- Methods:
  - Rocks have a higher thermal inertia than fine-grained regolith, leading to multiple temperatures in the same field of view (Fig. 1).
  - Larger rocks are warmer at the beginning of the night than small rocks and cool at different rates over the course of the night.

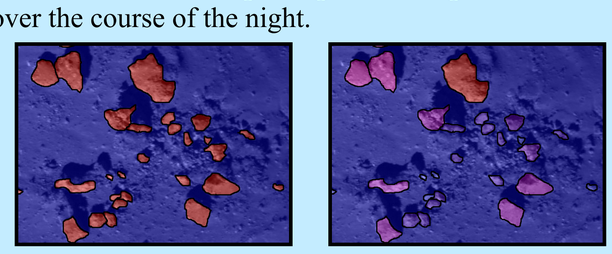

Figure 1. Cartoon of a section of the lunar surface from Diviner's perspective just after sunset (left) and later in the night (right). Red indicates hot and blue indicates cold.

Methods

- We model the diurnal temperature curve for a half hemisphere of rock embedded in regolith considering radii of 1 cm, 10 cm, and 1 m, at latitudes of 0º, 30º, and 60º using COMSOL multiphysics (Fig. 2).

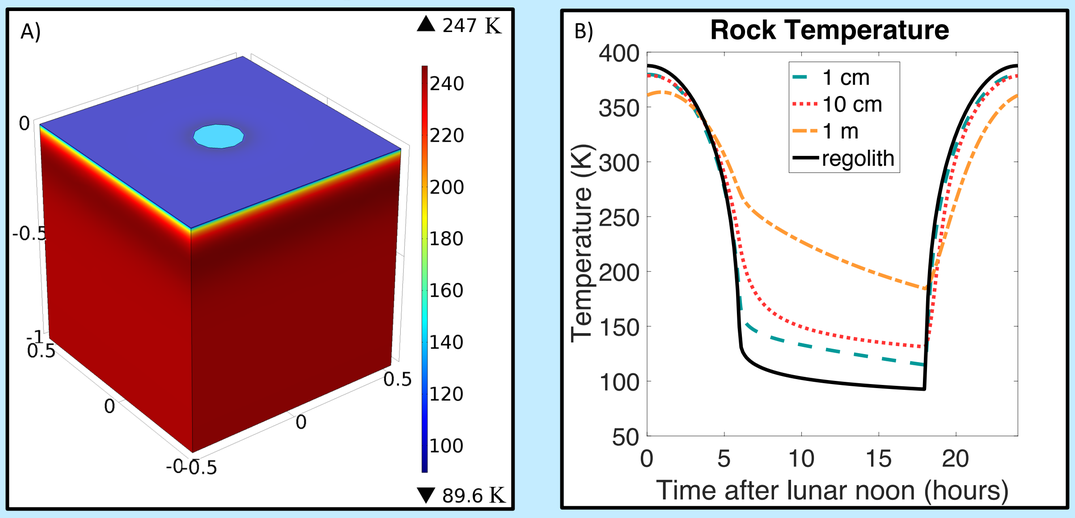

Figure 2. A) An example of the model set up showing a snap shot of the temperature at midnight. This example is of a half hemisphere of rock with a radius of 10 cm embedded in 1 cubic meter of regolith. B) The temperatures of regolith and half hemispheres of rocks (radii 1 cm, 10 cm, and 1 m) over the course of one lunar day.

- Assume the rock size frequency distribution can be described an exponential function:

$$F(D) = ke^{-qD}$$

  where F is the cumulative fractional area covered by rocks of size D or larger, k is the total fractional area covered by rocks, and q is the exponential factor which governs the rate of drop-off in the exponential function at large rock sizes [2].
- Apply the method of least squares to solve for k and q that best match the nighttime radiance observed at multiple times and multiple spectral channels using rock temperatures calculated with 3D models.

Figure 3. Model radiance expected for an area with 10% coverage by 10 cm sized rocks (red lines), 10% coverage by 1 m sized rocks (orange lines) and regolith with no rock coverage (black lines) at (A) 3 hours after sunset and (B) 10 hours after sunset.

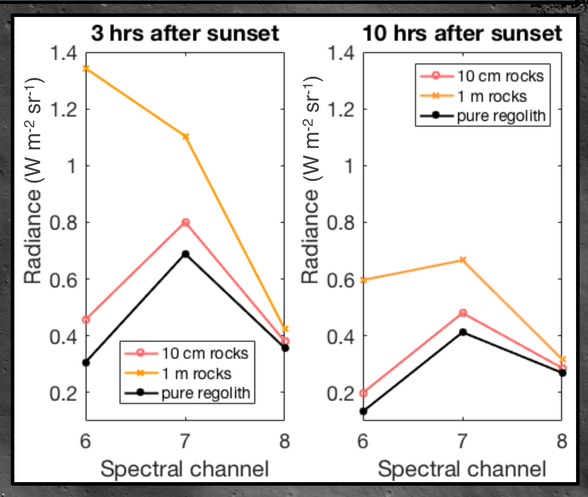

National Aeronautics and Space Administration

Jet Propulsion Laboratory
California Institute of Technology
Pasadena, California

www.nasa.gov

Results

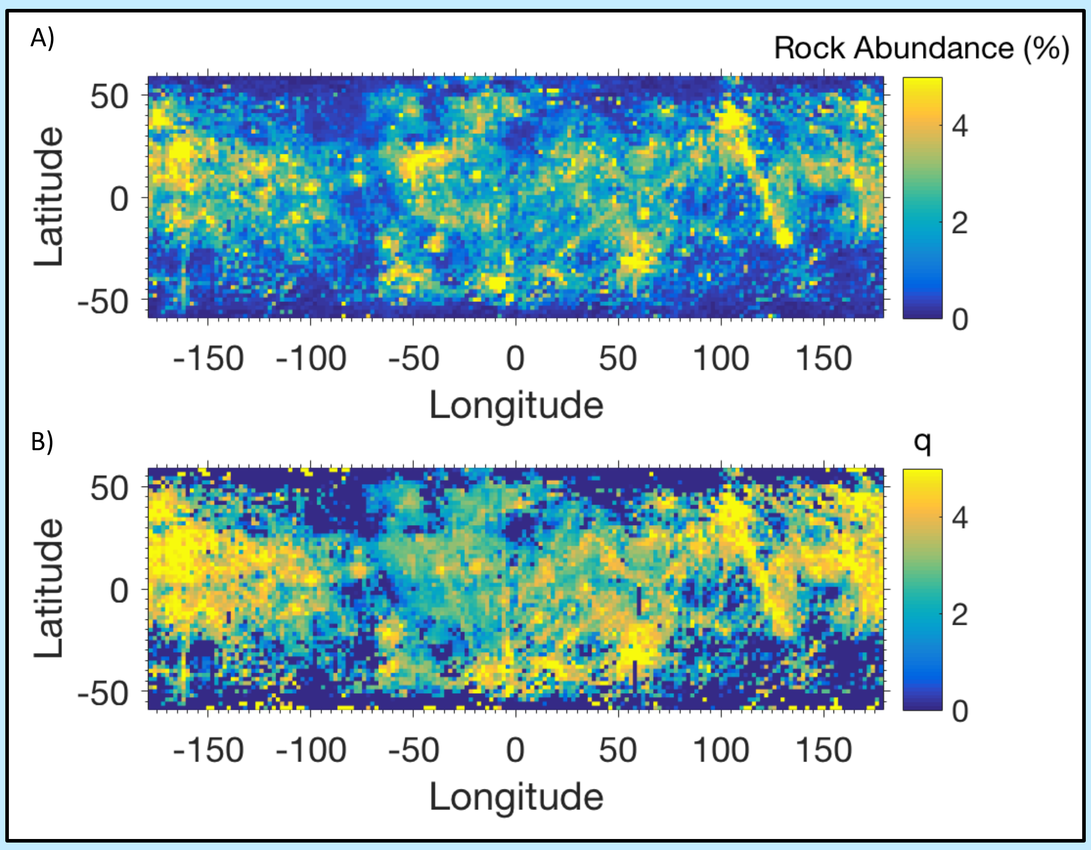

Figure 4. Preliminary lunar rock abundance map (percent of surface covered by rocks) (A) and preliminary map of the exponential factor, q, (B) where a higher q indicates relatively fewer large rocks. Diviner data has a resolution of up to 128 pixels per degree. Our preliminary results use this data binned to a lower resolution of 0.5 pixels per degree.

Interpretations and Conclusions

- By considering a range of rock sizes we are able to detect the contribution of rocks orders of magnitude smaller than previously possible.
- Notably, previous work (Fig. 5) showed low rock abundances in the lunar highlands, but we find local areas of high rock abundance in both the highlands and the maria.
- The rock size distribution map (Fig. 4B) shows that the lunar maria have more large rocks (lower q) relative to the lunar highlands (see Fig. 6 for comparison). This is consistent with the highlands older age and thus longer history of bombardment.

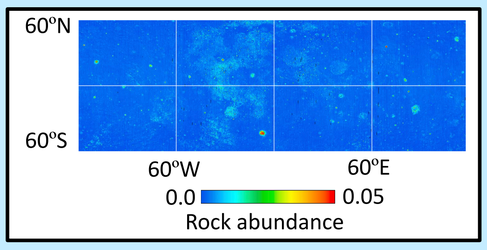

Figure 5. Rock abundance map from previous work using a 1D model to calculate rock temperature [1]. By including rocks of a range of sizes (as small as 1 cm), we find a higher rock abundance (Fig. 4A) and can distinguish regions with a relatively higher number of small rocks (Fig. 4B).

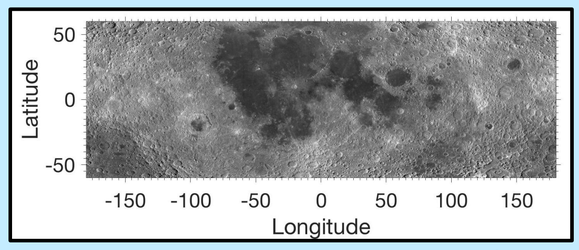

Figure 6. Lunar Reconnaissance Orbiter (LRO) Wide Angle Camera (WAC) global mosaic. Darker areas are the younger lunar maria and lighter areas are the older lunar highlands. Our results (Fig. 4B) show that the lunar maria have more large rocks relative to the lunar highlands.

Future work

- Model diurnal temperature curves for more rock sizes and latitudes.
- Validate the method by counting rocks in high resolution images from the Lunar Reconnaissance Orbiter Camera (LROC) at several locations and Apollo landing sites.
- Apply algorithm to full resolution Diviner data to produce higher resolution global maps.
- Produce global maps of rocks in different size ranges.

References

[1] Bandfield, J. L. et al. (2011) JGR, Vol. 116, E00H02.
[2] Golombek and Rapp (1997) JGR, Vol 102, NO. E2, 4117-4129.

Poster No. P-6

Venus surface emissivity from VIRTIS near infrared data and Magellan altimetry

Author: Nils Mueller (3223)
Co- Authors: Sue Smrekar (3223), Con Tsang (SWRI, Boulder, USA) , Dan Nunes (3223), Jörn Helbert (DLR, Berlin, Germany),

Introduction and Problem

- VIRTIS on Venus Express observed surface thermal emission at 1.02 micron
- Magellan altimetry constrains surface temperature and atmosphere column height
- Together this constrains surface emissivity
- Magellan altimetry of tesserae is a kilometer off in places, low emissivity could be an artifact

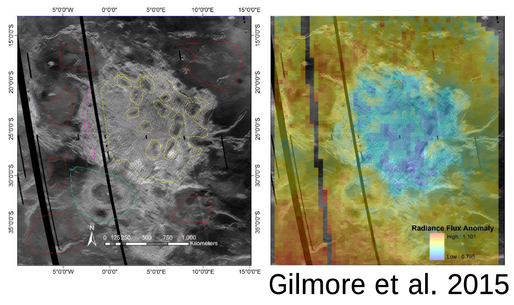

Gilmore et al. 2015

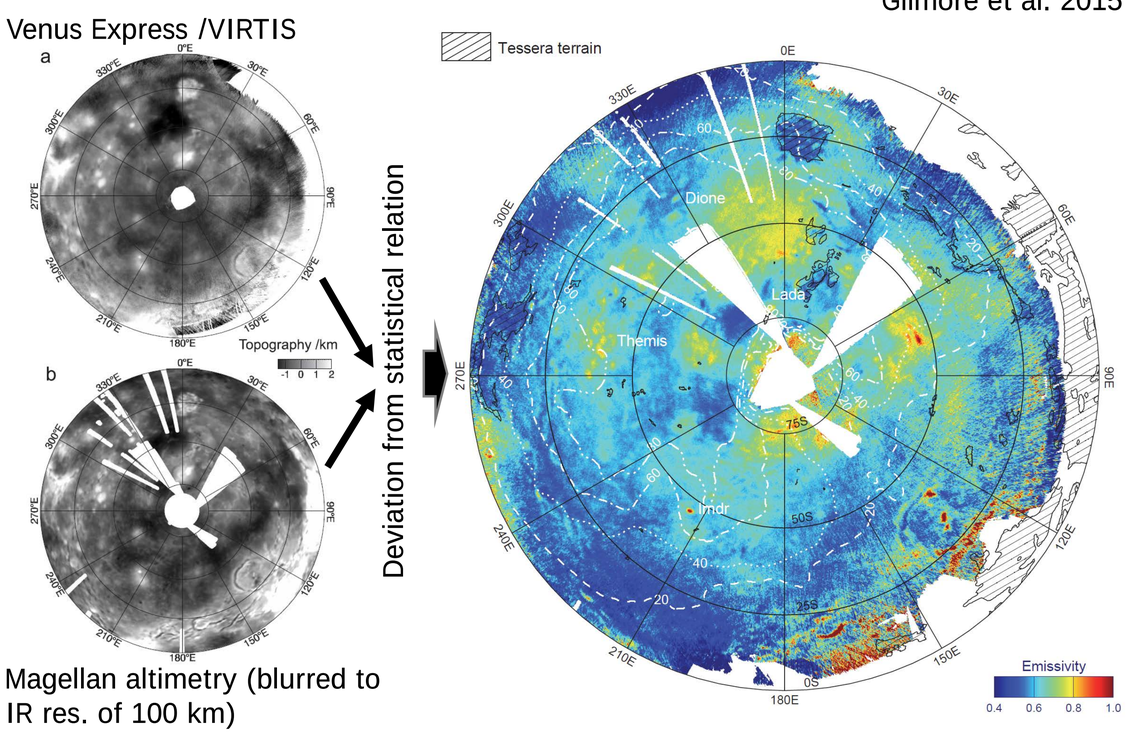

Magellan altimetry (blurred to IR res. of 100 km)

- Do tessera have a different composition than plains?
- Could tessera plateaus be analogues of Earths continental nuclei, felsic rock formed in the presence of an ocean?

Preliminary Results / Outlook

1. Data set of 25 Million VIRTIS thermal emission spectra
   - corrected for instrumental artifacts
   - To do: exclude data with questionable topography data
2. Atmospheric radiative transfer model
   - Parameters fitting data statistics (continuum opacity, average cloud opacity)
   - To do: improved spectral registration
   - To do: fit individual spectra: emissivity, local clouds, H2O
3. Stereo topography data
   - Data for test region
   - To do: tie into altimetry dataset for emissivity retrieval

References

- Gilmore et al. (2015) VIRTIS emissivity of Alpha Regio, Venus, with implications for tessera composition. Icarus 254 (2015) 350–361
- Kappel et al. (2012) Refinements in the data analysis of VIRTIS-M-IR Venus nightside spectra Adv. in Space Res., 50, 228–255.
- Tsang et al. (2008) A correlated-k model of radiative transfer in the near-infrared windows of VenusJ. Quant. Spectrosc. Radiat. Transf., 109, 1118–1135.

Methodology

1. Use three bands instead of just one

- Three windows in VIRTIS range observe the surface
- Windows at 1100 and 1180 nm are narrower than 1020 nm
- Weaker surface signal
- Additional corrections required:
  - Straylight and detector nonlinearity following Kappel et al. (2012)
  - Spectral registration (band shift and width)

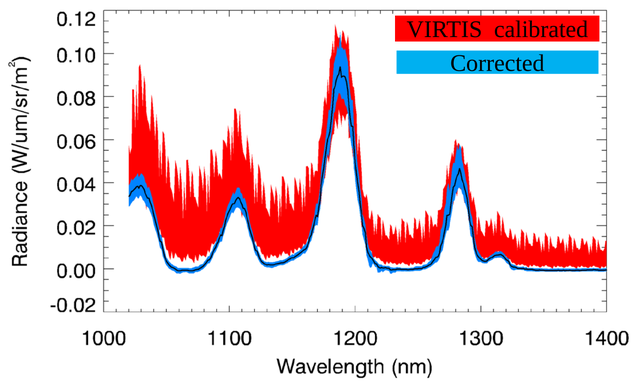

2. Better modeling of data, physics fitting statistics

Atmospheric Radiative Transfer Model:

- Tsang et al. (2008)
- Look up tables of synthetic spectra with parameters
  - Collision induced absorption (CIA) coefficient
  - Cloud opacity
  - Topography (surface temperature and pressure)
  - Surface emissivity
  - Water vapor

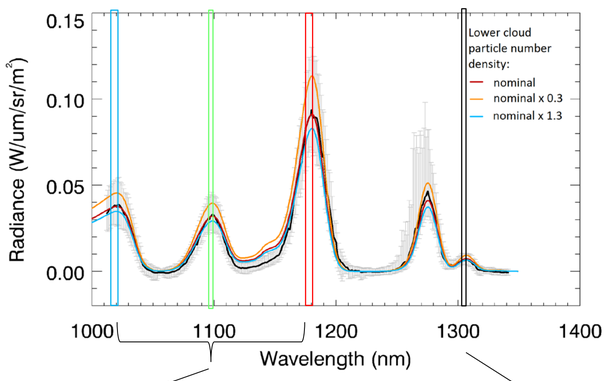

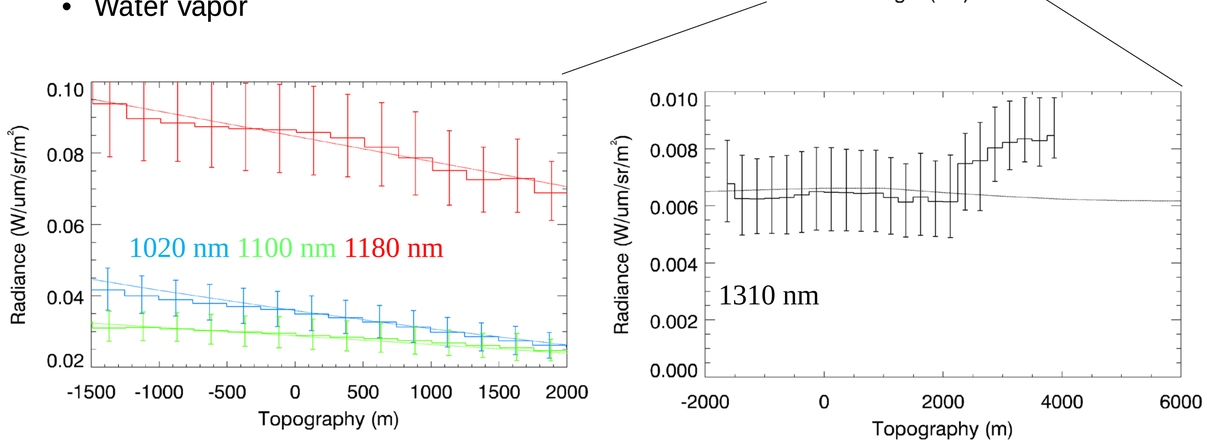

Solid: Data. Dashed: Model. Surface windows show trend with topography fitted by varying CIA coefficient. Coincidental correlation of cloud opacity (1310 nm) and topography still needs to be accounted for. **Does the tessera anomaly match an error in topography?**

3. Better topography data (where available)

- Magellan stereo SAR data provides better topography resolution
- Low vertical accuracy: Has to be tied into radar altimetry
- Unreliable in areas with little contrast
- Tie in manually in plains (good for altimetry) with some contrast (good for stereo)
- Test location: Xi Wang Mu tessera

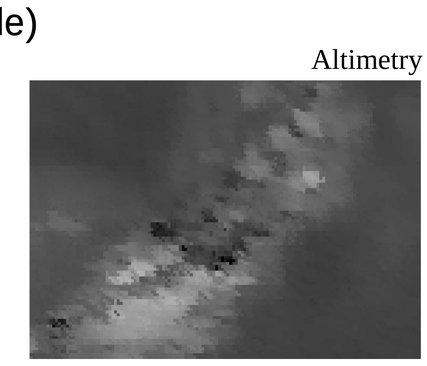

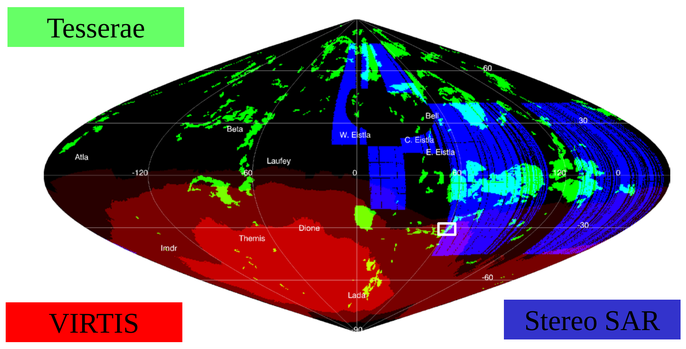

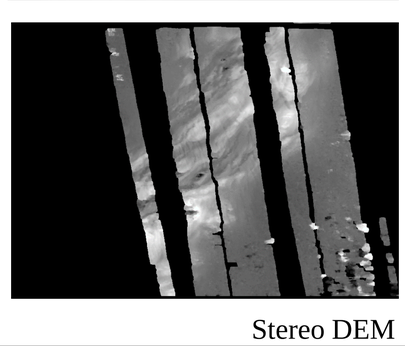

National Aeronautics and Space Administration
Jet Propulsion Laboratory
California Institute of Technology
Pasadena, California

www.nasa.gov

Poster No. P-7

National Aeronautics and Space Administration

High-resolution Goldstone Radar Imaging of Near-Earth Objects

Author: Shantanu P. Naidu (322)
Co-Authors: L. A. M. Benner (322), M. Brozovic (392), J. D. Giorgini (392), J. S. Jao (332), C. G. Lee (332)

Introduction

Radar is arguably the most powerful ground-based tool for refining the orbits and characterizing the physical properties of near-Earth objects. Radar routinely provides decameter resolution images of objects that cannot be resolved using any other ground-based technique. This allows us to estimate shapes, sizes, spin states, masses, densities, and other physical properties of the targets. Such detailed characterization can enable or enhance human and robotic missions. As part of our ongoing radar survey, we used the 70-m DSS-14 and the 34-m DSS-13 antennas at Goldstone to observe 46 near-Earth objects since 2015. The observations included 22 potentially hazardous asteroids and 11 potential human mission targets. We discovered three binary asteroids and two contact binary asteroids.

Goals:

- Survey the population of near-Earth asteroids using radar
- Estimate sizes, shapes, spin states, and other physical properties of the radar targets

Methods:

- Identify and prioritize targets
  - Mission targets, potentially hazardous objects, and high signal-to-noise ratio targets are given priority
- Plan the observing strategy
  - Identify observing telescopes (DSS-14, DSS-13, Green Bank Telescope, Arecibo)
  - Design observing set-ups (radar waveform, signal processing parameters)
- Schedule tracks based on expected signal-to-noise ratios, sky coverage, and time availability
- Refine target trajectories on the fly to reduce smearing and obtain sharper images as well as update observing set-ups based on new information
- Use data products to analyze physical properties of targets

Results:

2015 TB145

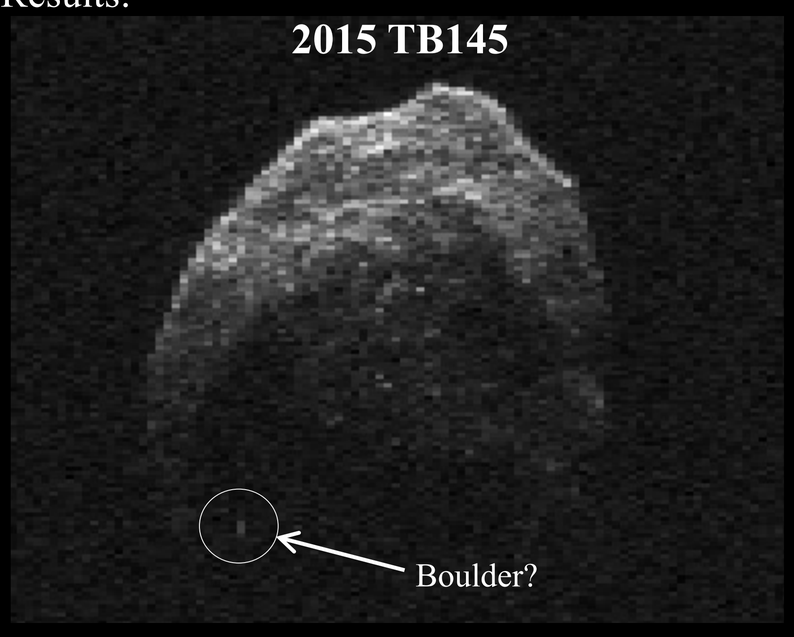

Fig 1. Telescopes: DSS-14 & GBT. Range resolution: 3.75 m/pixel. Target size: ~600 m. Spin period: ~3 h. This asteroid came within 1.3 lunar distances of Earth on Oct 31, 2015, three weeks after being discovered. Radar images show evidence for boulders, which are of interest to space missions such as the Asteroid Redirect Mission.

Comet P/2016 BA14

Fig 2. Telescope: DSS-14. Range resolution: 7.5 m/pixel. Target size: ~1 km. Spin period: 35-40 h. These are the highest resolution Goldstone images of a comet. There is no evidence of coma in radar data but there are many subtle surface features that are consistent with past activity.

2004 BL86 (Binary asteroid)

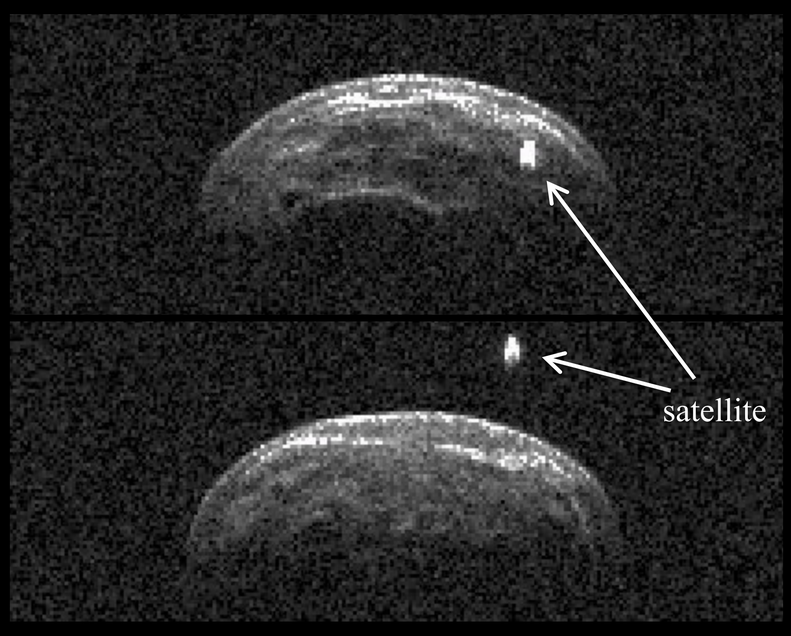

Fig 3. Telescopes: DSS-14 & GBT. Range resolution: 3.75 m/pixel. Target dimensions: Primary ~280 m, satellite ~70 m. Components separated by ~340 m. Primary spin period: 2.6 h.

2011 UW158

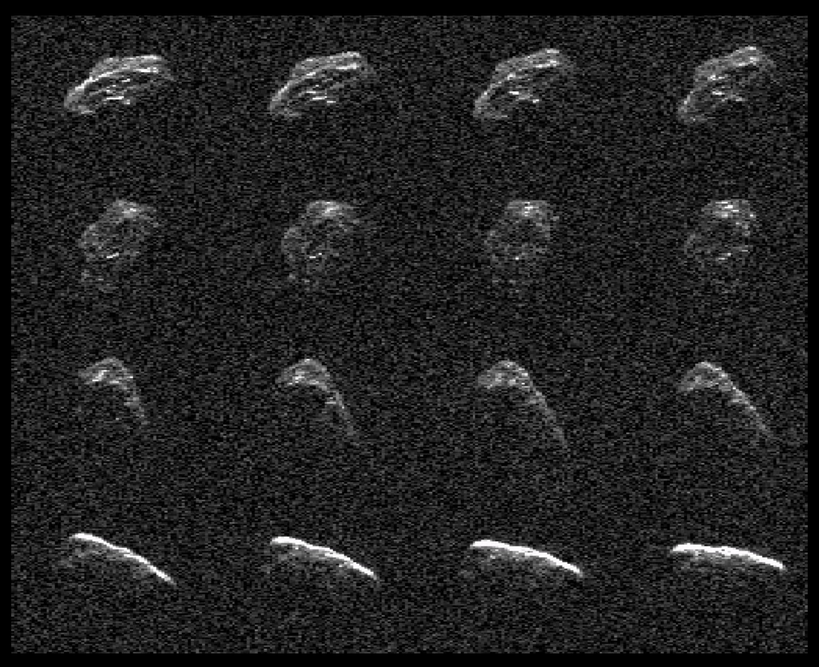

Fig 4. Telescopes: DSS-14 & GBT. Range resolution: 7.5 m/pixel. Target dimensions: ~600 m x 300 m. Spin period: ~37 minutes. This is one of the fastest spinning objects in its size range (> 100 m). Almost all other known asteroids larger than 100 m have spin periods > 2.1 h. The fast spin suggests that there is some cohesion holding the asteroid together. There are signatures of flat regions, linear parallel ridges, as well as boulders. Existence of boulders on such a fast spinning object would have implications on cohesive forces on the surface.

2009 DL46 (Contact binary)

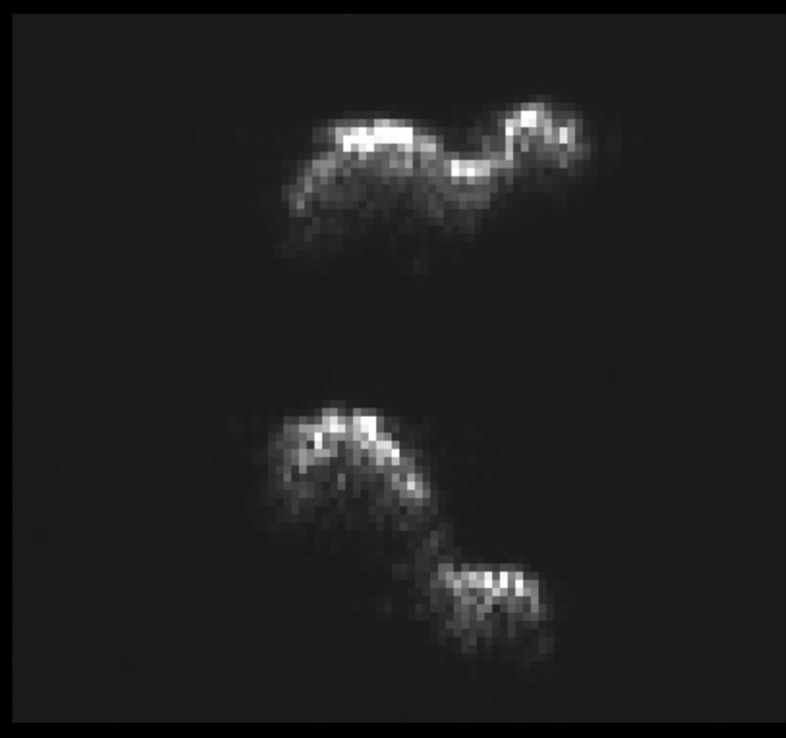

Fig 5. Telescopes: DSS-14/GBT. Range resolution: 1.875 m/pixel. Target dimensions: ~110 m x 60 m. Components are about 70 m and 40 m. Spin period: ~250 h. Is this the slowest known spin period among objects < 100 m?

2015 HM10

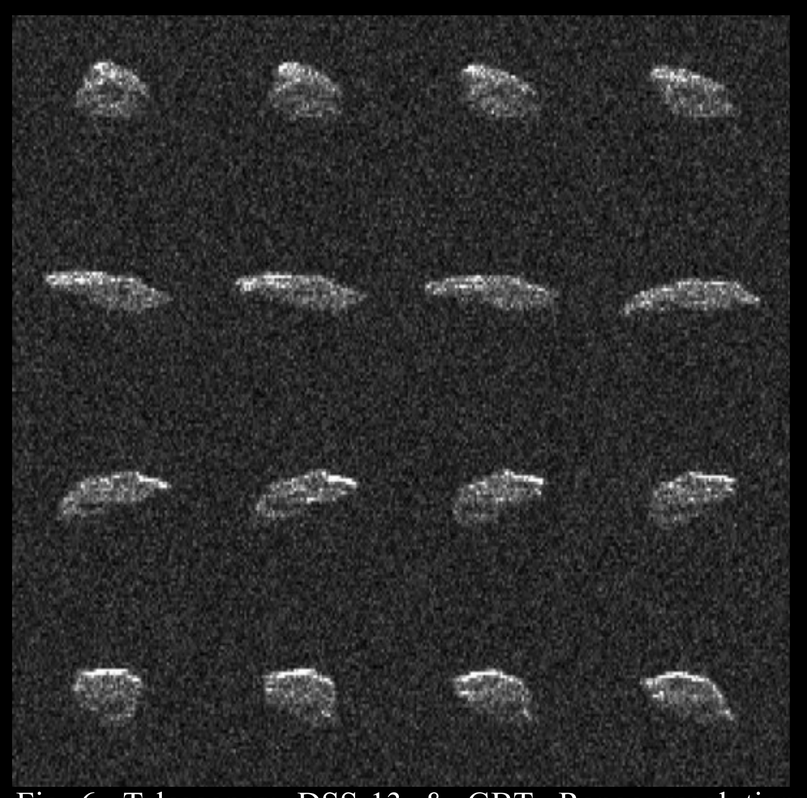

Fig 6. Telescopes: DSS-13 & GBT. Range resolution: 1.875 m/pixel. Target dimensions: 80 m x 40 m. Spin period: ~22 min. Object displays flat regions and ridges which might provide clues to the break up mechanisms of asteroids.

National Aeronautics and Space Administration

Jet Propulsion Laboratory
California Institute of Technology
Pasadena, California

www.nasa.gov

Poster No. P-8

National Aeronautics and Space Administration

Studying the Differences Between Comet Populations with WISE/NEOWISE

Principal Investigator: Dr. Emily Kramer (3224)

Co-Investigators: James Bauer (3224)

Introduction: Why Study Comets?

- Comets are mostly unaltered since formation, but have undergone some changes due to different heating processes
- Long period comets (LPCs) and short period comets (SPCs) are thought to originate in regions of the protoplanetary disk
- By studying a large number of SPCs and LPCs, population-wide characteristics can be determined, and any differences between the populations can be elucidated

Introduction: WISE/NEOWISE Mission

- **NEOWISE** = **N**ear **E**arth **O**bject **W**ide-field **I**nfrared **S**urvey **E**xplorer
- All-sky survey, terminator following polar orbit
- Four infrared detectors: 3.4, 4.6, 12, and 22 μm (hereafter W1, W2, W3, and W4, respectively)
- Prime mission:
  - Cryo: Jan. – Sep. 2010 W1 – W4
  - Post-cryo: Sep. 2010 – Jan. 2011 W1, W2
- Reactivated mission:
  - December 2013 – present W1, W2

Comets in WISE/NEOWISE

- **The NEOWISE augmentation to the WISE mission has provided the largest survey of comets in the infrared to date**
  - 163 comets during prime mission, 21 discoveries
  - >100 comets (as of July 2016) during reactivated mission, 8 discoveries (to date)
- Substantial fraction of the known population, allowing characterization to be done across a wide range of objects
- Survey is non-targeted: allows for population-wide characterization to be done with fewer biases than with a targeted survey
- Each comet serendipitously observed multiple times, individual images stacked to increase signal-to-noise ratio

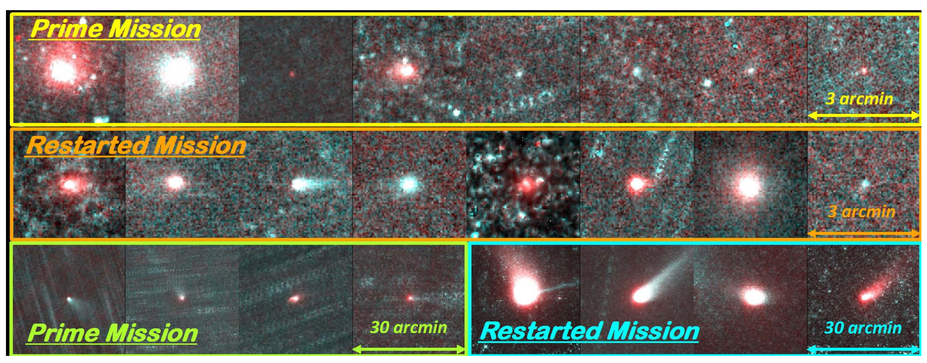

Figure 1: A selection of comets detected by NEOWISE (shown here with W2 mapped to red, and W1 mapped to both blue and green)

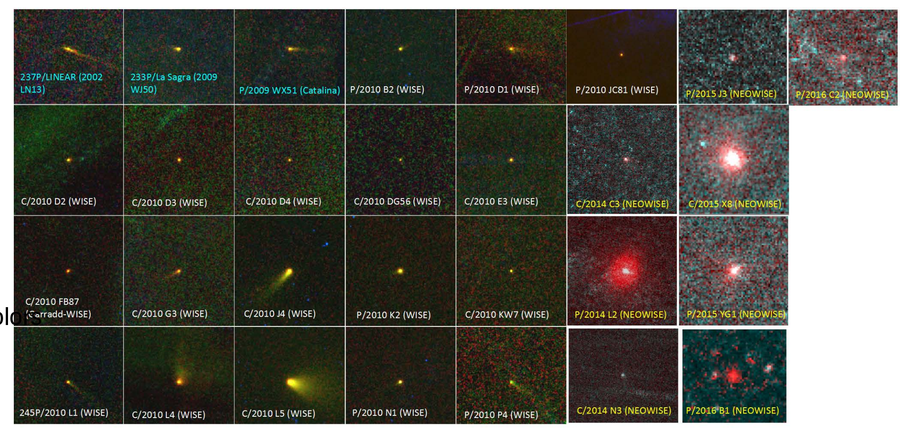

Figure 2: Discovery images of WISE/NEOWISE comets shown in 3-color

Nucleus Sizes of WISE-discovered Comets

- Model coma is subtracted from data, extracted nucleus signal fit to NEATM
- **WISE-discovered long period comets (LPCs) are on average bigger than short period comets (SPCs)**

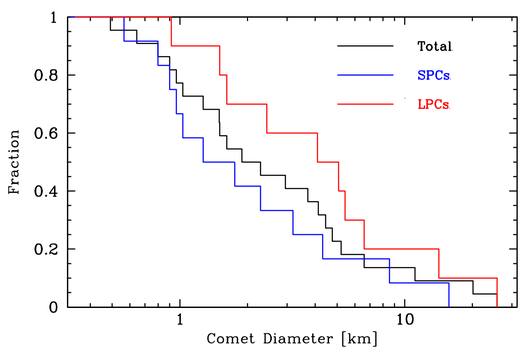

Figure 3. The cumulative size distribution of the nuclei of comets discovered by WISE/NEOWISE

Afρ and *εfρ*, Measures of Dust Quantity

- Commonly used method to characterize the quantity of dust visible at a particular wavelength (*εfρ* in infrared, *Afρ* in visible)
- **LPCs and SPCs show similar *εfρ* values (A), and the relationship between *Afρ* and *εfρ* seems to markedly change beyond ~4 AU (B)**

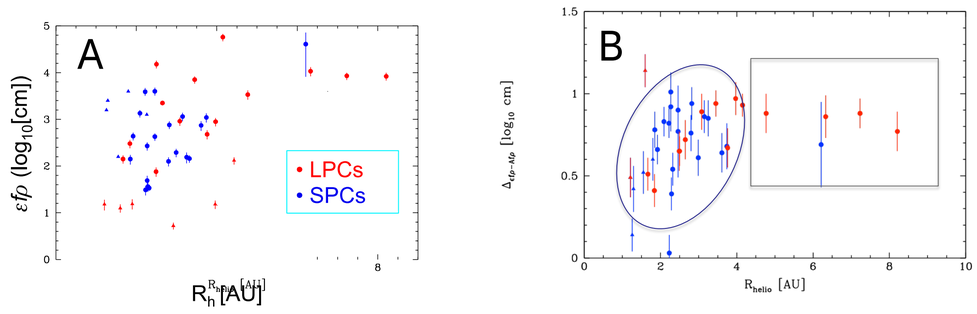

$CO + CO_2$ Production Rates

- Fit a Planck function to W3 and W4, and solar spectrum to W1 for each comet
- Determine predicted flux for W2, excess flux in W2 (4.6 μm band) due to $CO+CO_2$
- **In our sample CO_2 production rates are similar for LPCs and SPCs (C), and show a clear R_h^{-2} relationship inside 4 AU when compared with *εfρ* (D)**

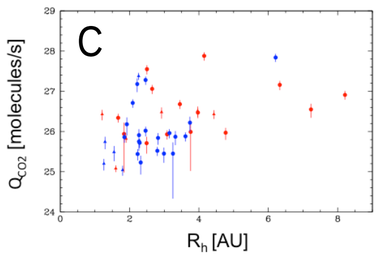

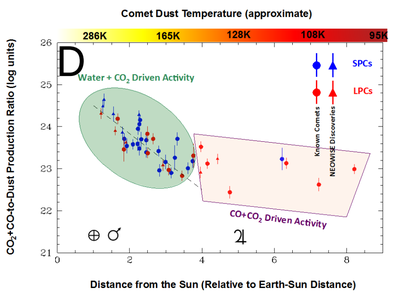

Dust Tail Modeling

- Dust tails modeled using syndyne-synchrone models, which parameterizes the motion of the dust with $\beta \equiv F_{rad}/F_{grav}$
- Novel tail fitting technique used to allow best-fit model to be chosen analytically
- **Most of the tails comprised of large (~mm to cm) sized particles (E) that were emitted near perihelion (F)**

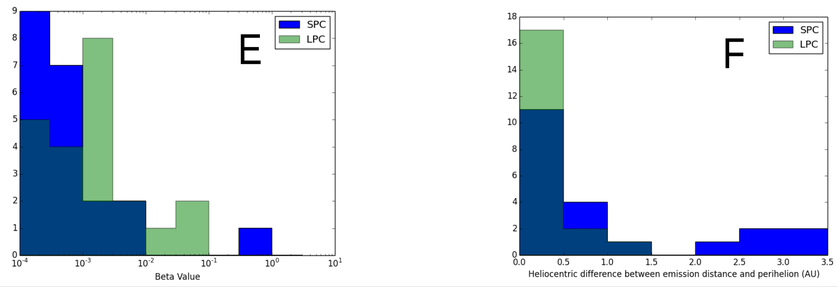

Interpretations and Conclusions

- The SPCs and LPCs observed by NEOWISE are, on average, very similar, except in terms of nucleus size
- This suggests that the two populations may have been drawn from the same primordial population, and SPCs may have been subsequently eroded away during perihelion passages
- This work will be extended to comets from the NEOWISE reactivation mission, increasing our sample size

National Aeronautics and Space Administration

Jet Propulsion Laboratory
California Institute of Technology
Pasadena, California

www.nasa.gov

Poster No. P-9

National Aeronautics and Space Administration

Dynamics of planetary ice layers with liquid water

Klara Kalousova (Jet Propulsion Laboratory, California Institute of Technology, 3225), **Christophe Sotin** (Jet Propulsion Laboratory, California Institute of Technology, 4000), **Dustin M. Schroeder** (Stanford University), **Krista M. Soderlund** (University of Texas at Austin)

Introduction

Ocean worlds of the outer solar system are icy moons with a deep water ocean. Assessing their potential habitability requires a better understanding of their thermal evolution and interaction of the deep ocean with the ice layers and the rocky core. For this purpose, we have developed a numerical model of two-phase convection that enables us to investigate the melting processes as well as heat and meltwater transport. With this tool we have investigated: (i) meltwater generation and transport within the high-pressure (HP) ice layer of Ganymede and (ii) radar attenuation within the outer ice I shell of Europa.

HP ice layer of Ganymede: Heat and water transport

- **no direct contact between silicates and water** (Figure 1)
- Can there still be a water/material exchange between the silicates and the ocean ?
- Key model parameters: ice viscosity, heat flux from the silicates, permeability of the HP ice

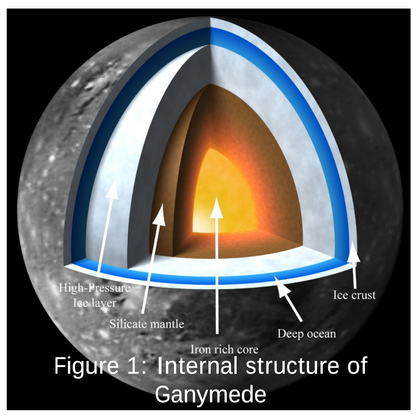

Figure 1: Internal structure of Ganymede

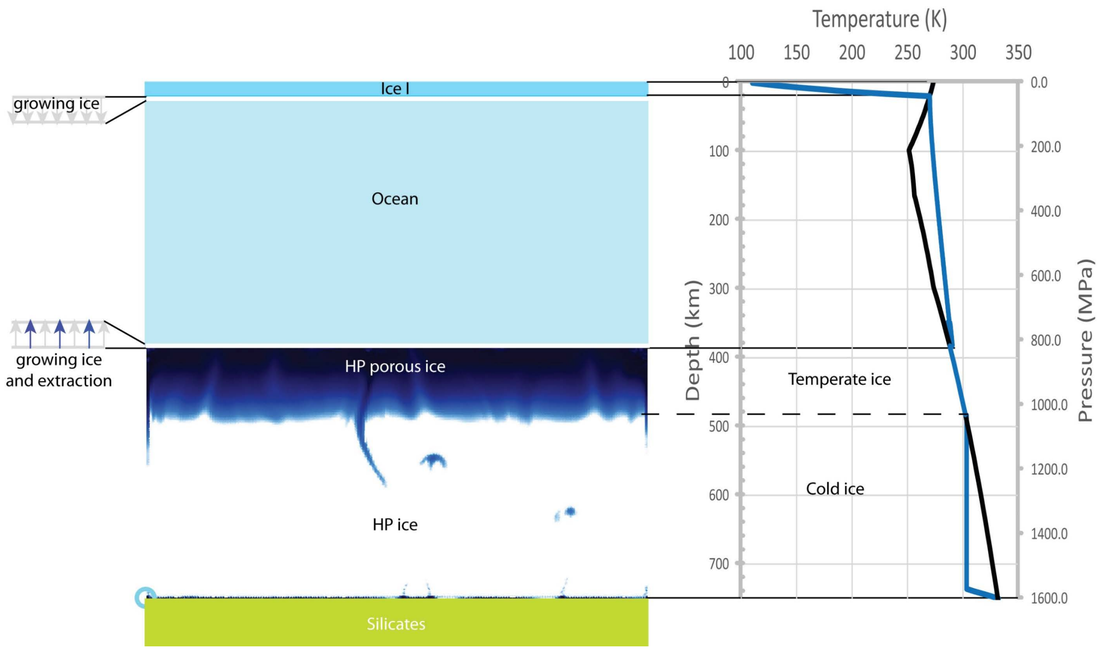

Figure 2: Schema of investigated processes: meltwater produced at the boundary with silicates is advected upwards by convection and then extracted into the overlying ocean by percolation.

- **Modeling results**:
  - Heat coming out of the silicate layer melts the ice at the bottom boundary
  - Presence of meltwater facilitates the upwelling of warm convective plumes
  - Cold ice ($T<T_{melt}$) within the lower part of the layer → water transported by convection
  - Temperate ice ($T=T_{melt}$) within the upper lid → water transported by percolation
  - Majority of water is extracted into the ocean
  - Onset time and vigor of convection governed by the ice viscosity (Figure 3)
  - Amount of generated meltwater governed by the heat flux from the silicate mantle
  - Water extraction efficiency governed by the HP ice permeability

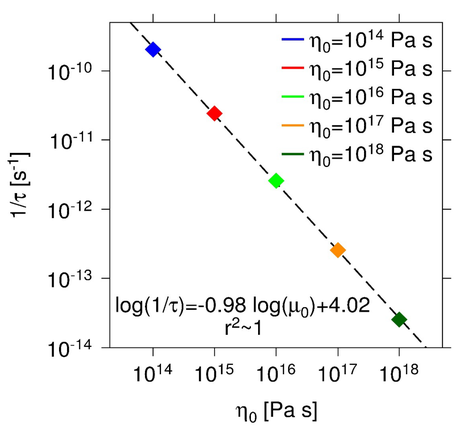

Figure 3: Linear instability growth rate $1/\tau$ inferred from the simulations as a function of viscosity. The dashed line shows the least squares linear fit.

Ice I shell of Europa: radar attenuation

- **direct contact between silicates and water** (Figure 4) → **habitability ?**
- Ice penetrating radar instruments of future Europa missions → investigation of **subsurface thermophysical structure**
- Radar signal attenuation in ice depends mainly on temperature → constraining the thermal structure of Europa's shell is of key importance for determining **radar performance**

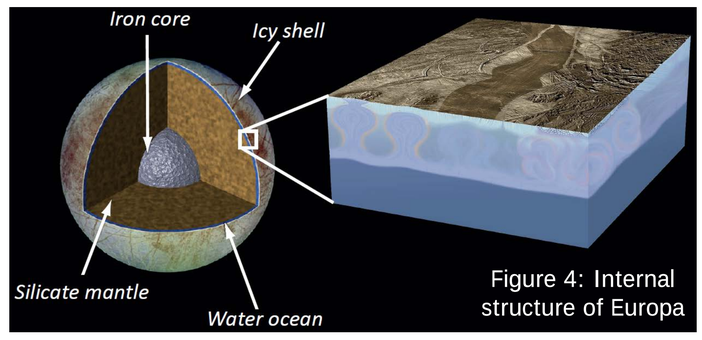

Figure 4: Internal structure of Europa

Approach: – numerical simulations → thermal state (convective / conductive) → evaluation of radar attenuation from temperature → penetration depth (att = 100 dB)

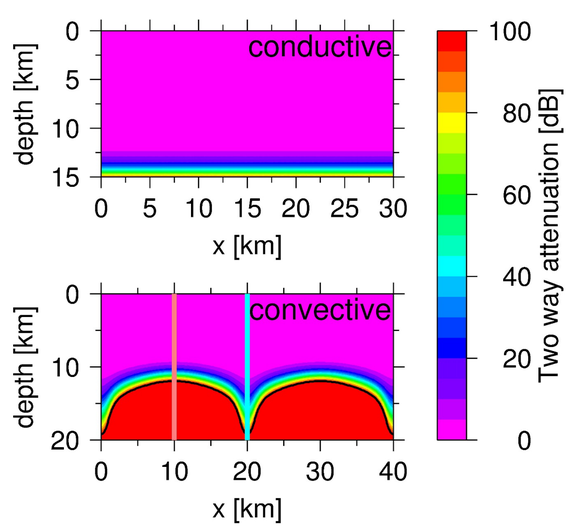

Figure 5: Radar attenuation in a conductive (top) and convective (bottom) shell. Red and blue columns in the bottom panel mark the hot and cold temperature profiles, respectively. Black line marks attenuation of 100 dB (penetration limit).

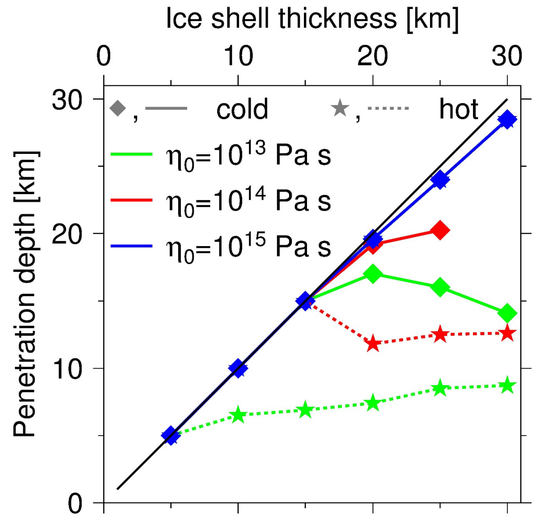

Figure 6: Penetration depth as a function of ice shell thickness for various viscosities and hot (dashed lines) as well as cold (full lines) profiles.

- **Modeling results**:
  - The maximum penetration depth varies laterally – deepest penetration possible through cold downwellings (Figure 5)
  - For all investigated shell thicknesses (5-30 km), the radar sounder will penetrate between 15% and 100% of the total ice I thickness
  - Direct ocean detection might be possible for shells of up to 15 km thick (Figure 6)
  - Penetration through most of the shell can constrain the deep shell structure through returns from deep non-ocean interfaces or the loss of signal itself
  - Surface heat flux of 20 to 30 mW m^{-2} was obtained from simulations

Summary

1. We have investigated meltwater generation and transport within the HP ice layer of Ganymede. Our results indicate that melting occurs mainly at the silicates/HP ice interface. Some melt can remain at this interface, but the majority of meltwater is transported towards the top boundary where it is extracted into the overlying ocean, possibly together with volatiles leached from the silicate mantle. (These results were presented at AGU in 2015 and a corresponding publication is being finalized for submission in Icarus).
2. We have studied radar attenuation within the icy shell of Europa in order to constrain the performance of future satellite-borne ice-penetrating radars. Our results indicate that a radar sounder should penetrate between 15% and 100% of the total shell thickness. Direct detection of the ice/ocean interface might be possible for shells of up to 15km. (Paper summarizing this research is now under review in JGR-Planets).

Acknowledgements: KK acknowledges support by the office of the JPL chief scientist.

National Aeronautics and Space Administration

Jet Propulsion Laboratory
California Institute of Technology
Pasadena, California

www.nasa.gov

Poster No. P-10

National Aeronautics and Space Administration

The near-surface electron radiation environment of Saturn's moon Mimas

Author: Tom Nordheim (3225) Advisor: K.P. Hand (4000)

Introduction: Saturn's inner mid-size moons are exposed to a number of external weathering processes, including charged particle bombardment and UV photolysis, as well as deposition of E ring grains and interplanetary dust. While remote sensing observations by several instruments onboard the Cassini spacecraft have revealed a number of weathering patterns across the surfaces of these moons [1][2][3][4][5], it is currently not entirely clear which external process is responsible for which observed weathering pattern. Here we focus on Saturn's moon Mimas and model the effect of energetic electron bombardment across its surface in order to better understand the remote sensing observations.

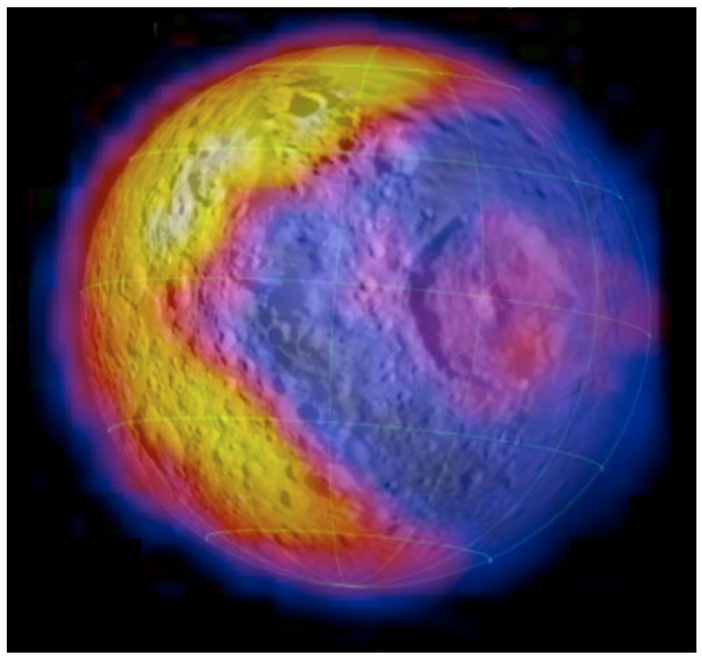

Night-time surface temperatures on Mimas. Image: C. Howett

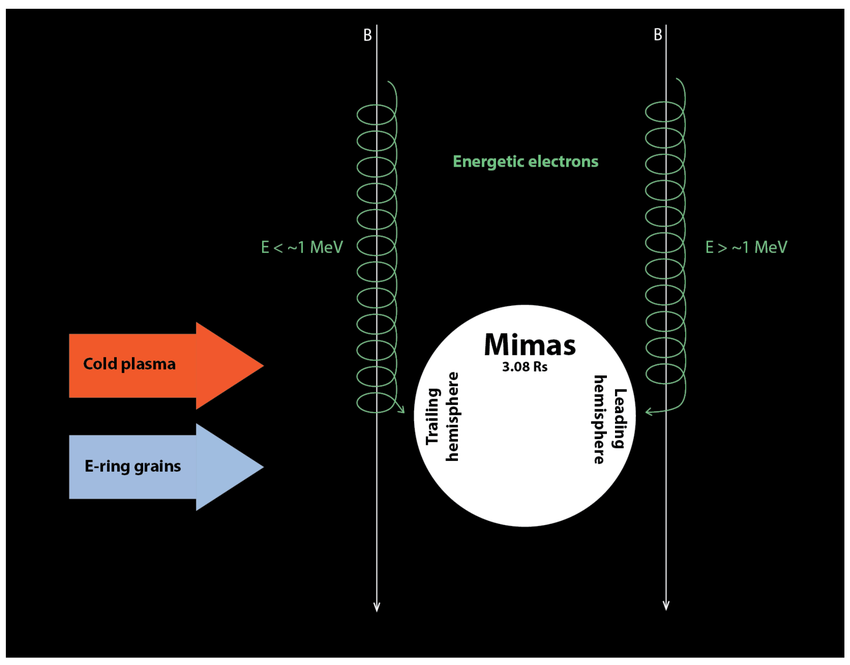

Space weathering agents bombarding the surface of Mimas

Method: To model the access of energetic electrons to different surface locations we used a guiding center, bounce-averaged approach which has previously been employed for the Jovian [6][7] and Saturnian moons [8]. The electron spectrum is based on averaged measurements from the Cassini Magnetospheric Imaging Instrument (MIMI) Low Energy Magnetospheric Measurement System (LEMMS) at a narrow corridor near the orbit of Mimas (~3.08 Rs) during the period 2004-2013.

Tracing results: Due to the motion of energetic electrons in the Saturnian magnetosphere, electrons with energies above 1 MeV will impact the leading hemisphere surface at low latitudes. Higher latitudes on this hemisphere, however, are only exposed to more energetic electrons that are lower in flux.

At the trailing hemisphere, only the most energetic electrons with energies near 1 MeV are capable of reaching low latitude regions on the surface. Higher latitudes are only bombarded by keV electrons which are not capable of penetrating far into the surface.

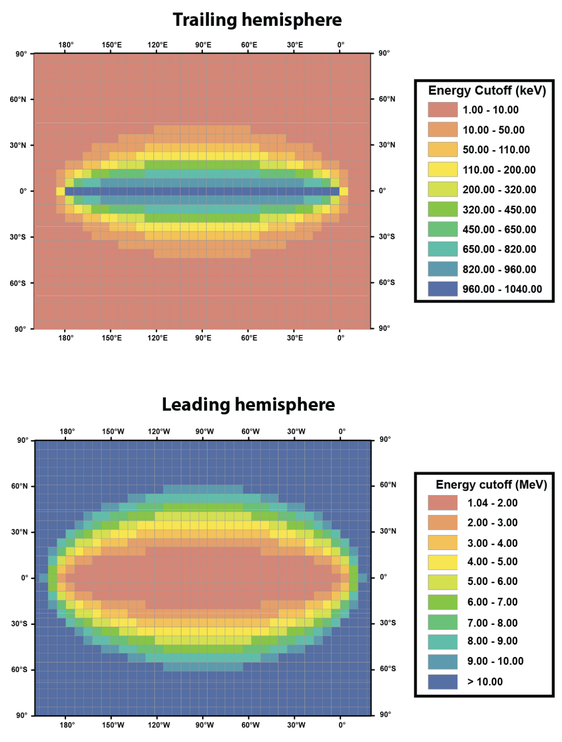

Energetic electron access to the trailing (top) and leading (bottom) hemispheres of Mimas.

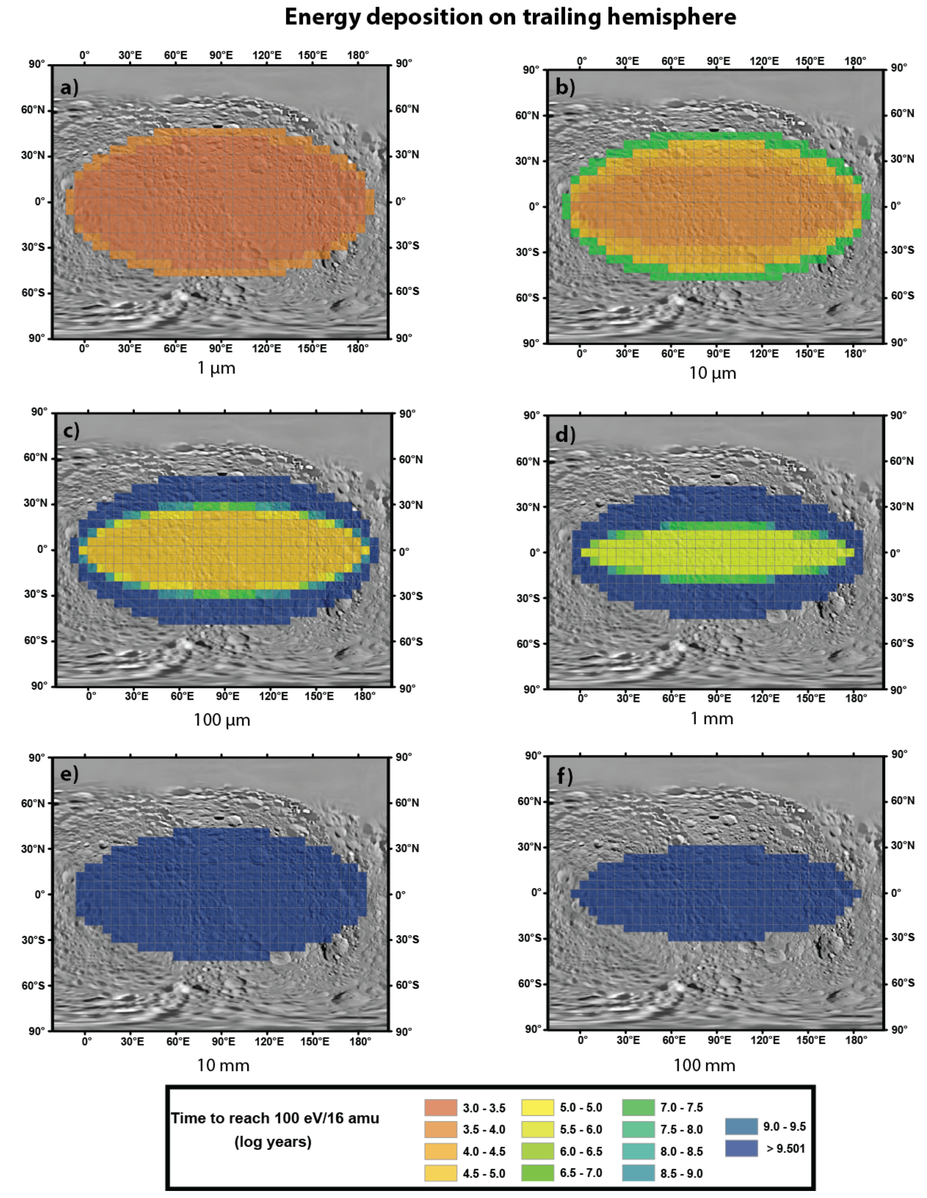

Time to reach a significant electron dose at several different surface depths

Deposition results: We predict a lens-shaped electron energy deposition pattern which extends down to ~cm depths at low latitudes near the center of the leading hemisphere. These results are consistent with previous remote sensing observations of a lens-shaped color anomaly[4] as well as a thermal inertia anomaly at this location [2][3][5]. At the trailing hemisphere, we predict a similar lens-shaped electron energy deposition pattern, whose effects have to date not been observed by the Cassini remote sensing instruments. Deposition of E-ring dust grains onto the trailing hemisphere does not appear to be a strongly competing effect.

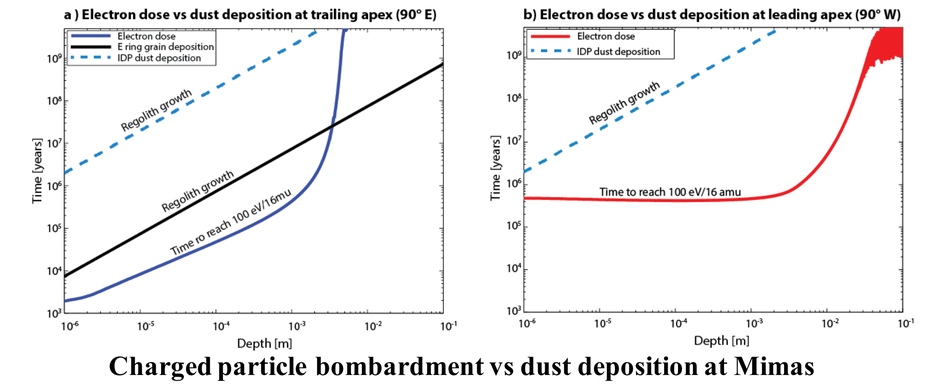

Charged particle bombardment vs dust deposition at Mimas

Conclusions: Our modeled energy deposition patterns for the leading hemisphere are consistent with an electron-generated origin for the observed equatorial lens. In addition, we also predict a similar lens-like electron bombardment feature at the trailing hemisphere.

References: [1] Hendrix, A.R. et al (2012) *Icarus 220*, 922–931. [2] Howett, C.J.A. et al. (2011) *Icarus 216*, 221–226. [3] Howett, C.J.A. et al. (2012) *Icarus 221*, 1084–1088. [4] Schenk, P. et al. (2011) *Icarus 211*, 740–757. [5] Filacchione, G. Et al (2016) *Icarus 271*, 292–313. [6] Patterson, G.W. et al. (2012) *Icarus 220,* 286–290. [7] Paranicas, C. et al. (2001) *Geophys. Res. Lett. 28*, 673–676. [8] Paranicas, C. et al. (2014) *Icarus 234*, 155–161. [9] Desorgher, L. et al. (2005) *Int. J. Mod. Phys. A 20*, 6802–6804. [10] Agostinelli, S. et al. (2003) *Nucl. Instruments Methods Phys. Res. Sect. A 506*, 250–303.

Poster No. P-11

National Aeronautics and Space Administration
Jet Propulsion Laboratory
California Institute of Technology
Pasadena, California

www.nasa.gov

National Aeronautics and Space Administration

Evolution of clathrate hydrates in presence of ammonia at Titan's crust conditions

V. Muñoz-Iglesias (3227)
T. H. Vu (3227), M. Choukroun (3227), R. Hodyss (3227), W. Smythe (3224), C. Sotin (4000)

Geochemical evolution at Titan's icy crust

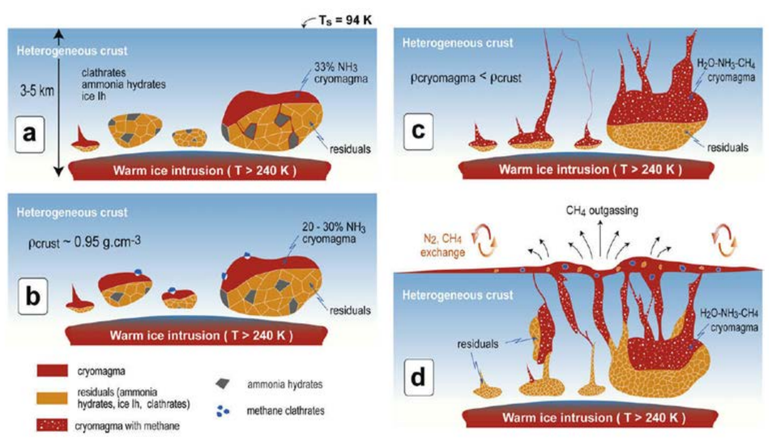

Model of cryomagma chamber on Titan (Choukroun at al. 2010)

- CH_4 replenishment process in the atmosphere → Origin of CH_4?
- Upper crust dominated by water ice, CH_4-, C_2H_6-clathrates and ammonia hydrates
- Dissolved NH_3 decreases significantly the melting temperature of water ice and clathrates → CH_4 release
- THF-clathrate: proxy for CH_4-clathrate at 0.1 MPa

Experimental study: Calorimetry

- Setaram BT 2.15 Calvet calorimeter

System: H_2O-THF-NH_3
Runs 77 K – 298 K
Heating rate: 0.1 K.min^{-1}

[NH_3] = 0 – 30 wt%
1:6 THF:H_2O to avoid water ice formation
(1:17 THF:H_2O in THF-clathrate)

[NH_3] = 5, 15, 30 wt%
THF:H_2O 1:X<17
THF:H_2O 1:X=17
THF:H_2O 1:X>17

Ammonia aqueous solution 30 wt%

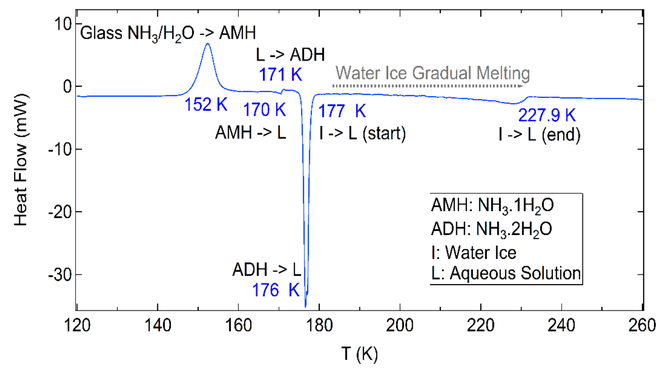

When the system H_2O-NH_3 is cooled, it forms ammonia hydrates

Results

Ammonia aqueous solution 30 wt%
THF:H_2O 1:X<17
THF:H_2O 1:X=17
THF:H_2O 1:X>17

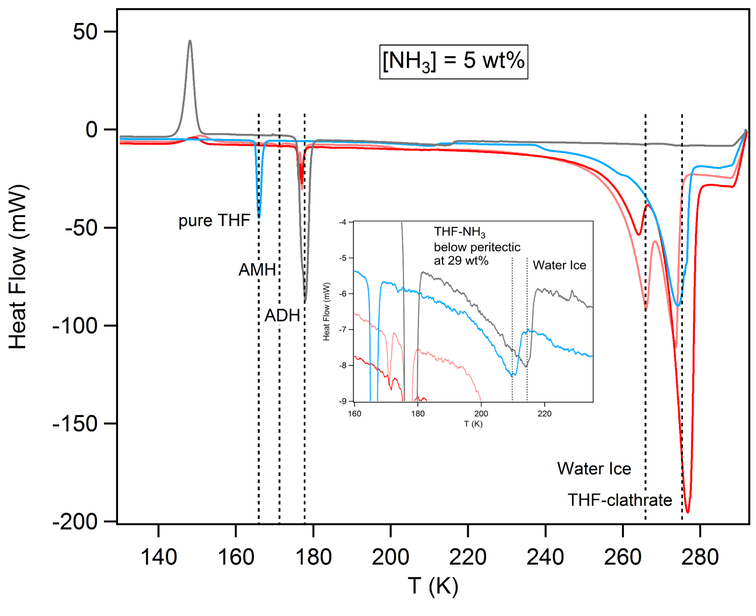

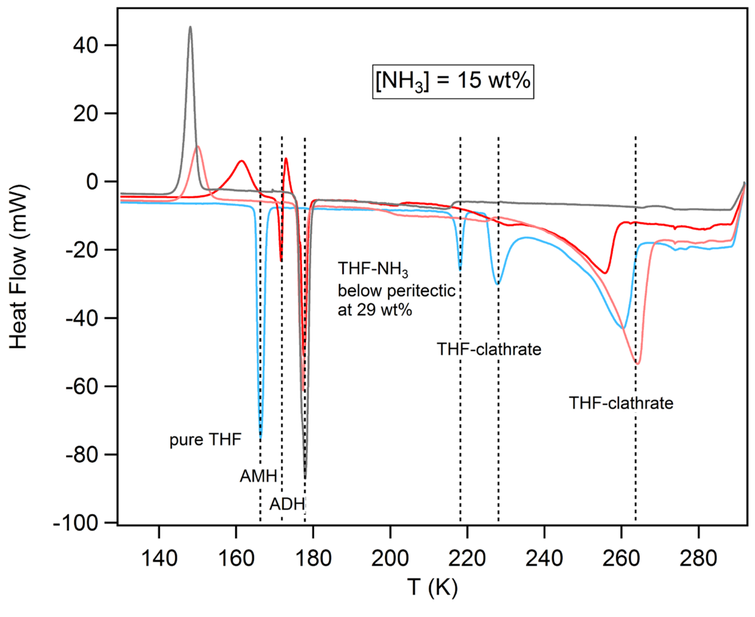

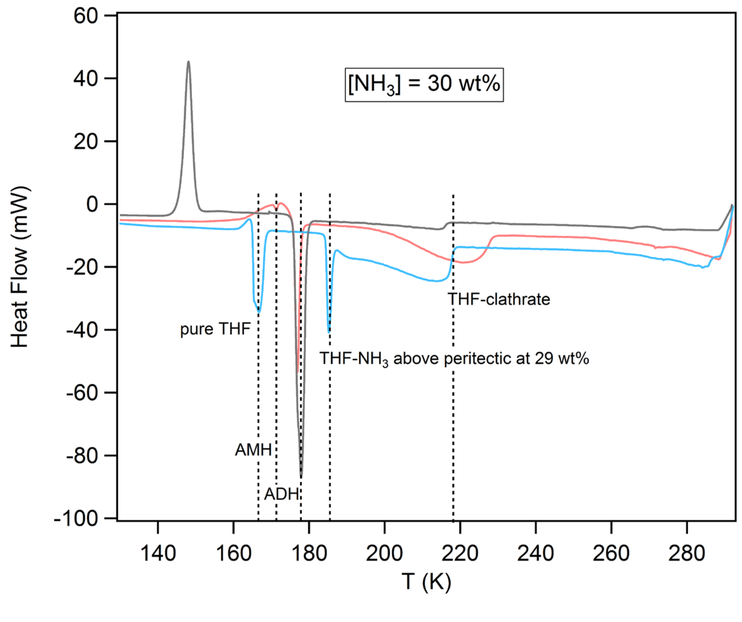

Phase diagram of the system H_2O-THF-NH_3 when THF is in excess

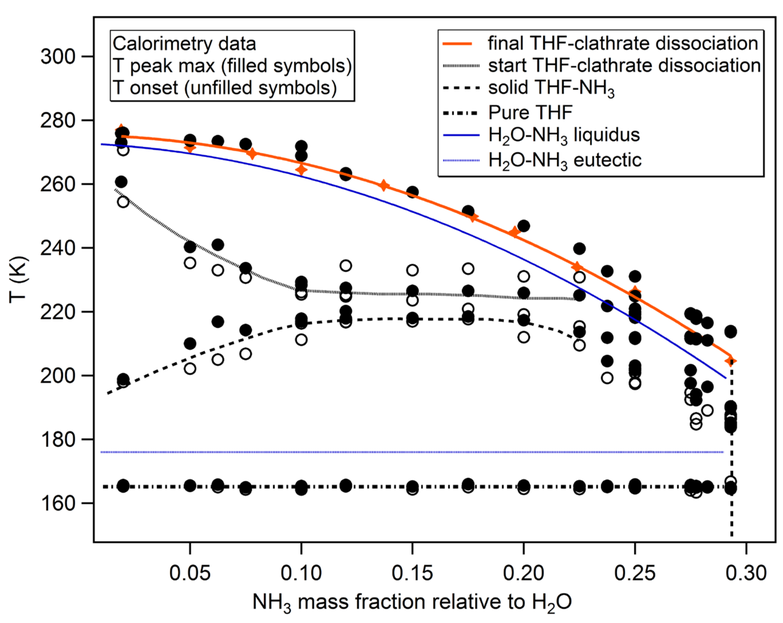

Partially miscible liquids → Temperature dependent phase separation: THF-clathrates in the NH_3-rich aqueous phase melt at lower temperatures than THF-clathrates formed in the THF-rich aqueous phase

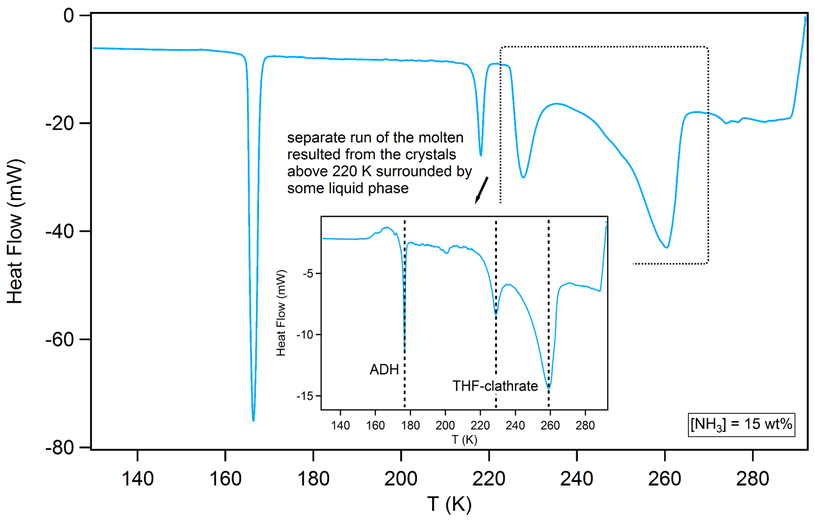

Discussion

Phases formed in the system THF-H_2O-NH_3 when the molar ratio H_2O:THF is 1:X < or > 17, which corresponds with the THF-clathrate stoichiometric ratio, and at NH_3 concentrations up to 30 wt%:

- **When X < 17**, THF is in excess; all the H_2O forms THF-clathrates, no ammonia hydrates are observed, and the excess THF interacts with NH_3 to form a NH_3-THF phase.

- **When X > 17**, the H_2O is in excess; the formation of ammonia hydrates, water ice and THF-clathrate is observed. Since under this condition, all available THF is trapped in the clathrate, no THF-NH_3 phase is observed.

In all the scenarios, the release of NH_3 (from the melting of THF-NH_3 solid or ammonia hydrates) promotes partial dissociation of THF-clathrates, which starts at much lower temperature the equilibrium dissociation of the clathrates.

Acknowledgments: This research is supported by an appointment to the NASA Postdoctoral Program at the Jet Propulsion Laboratory, California Institute of Technology, administered by Universities Space Research Association (USRA) through a contract with NASA. Support from the NASA Outer Planets Research program and government sponsorship acknowledged.

National Aeronautics and Space Administration
Jet Propulsion Laboratory
California Institute of Technology
Pasadena, California

References: [1] Tobie et al. (2006) Nature, 440, 61-64. [2] Lunine J. I. et al. (2009) Titan from Cassini-Huygens, Ch. 3, 35-59. [3] Kargel J.S. (1992) Icarus, 100, 556-574. [4] Sloan E.D. and Koh C.A. (2008) Clathrate hydrates of natural gases, 3rd ed. CRC Press, Boca Raton, FL. [5] Choukroun M. et al. (2010) Icarus, 205, 581-593. [6] Niemann H. B. et al. (2010) JGR, 115, E12006. [7] Lavvas P. P. et al. (2008) Planet. Space Sci., 56, 1103-1111. [8] Vu T. H. et al. (2014) J. Phys. Chem. B, 118, 13371-13377. [9] Prasad P. S. R. et al. (2007) Spectrochim. Acta A, 68, 1096-1100.

www.nasa.gov

Poster No. P-12

National Aeronautics and Space Administration

NEW EXPERIMENTAL PLATFORM TO CONSTRAIN THE CHEMICAL COMPOSITION OF TITAN'S LAKES.

Author: Ahmed Mahjoub (3227)
Mathieu Choukroun (3227), Christophe Sotin (4000), Rob Hodyss (3227), Martin Bramatz (382J)

Overview: While Cassini has provided a wealth of information regarding the distribution of liquid deposits on Titan, it has provided only the most basic information regarding their composition and role in Titan's volatile cycle. We have developed a new experimental setup designed to study the composition of Titan's lakes in equilibrium with the atmosphere. In this system, we can prepare a variety of hydrocarbon mixtures (primarily methane, ethane, and propane) in the gas phase, and condense them under Titan-simulated conditions (1.5 bar nitrogen pressure, 92 K). This experimental setup will also provide a 10 Litre volume of liquid hydrocarbons to test the operation of hardware (small instruments, components) under Titan lakes conditions.

Titan's lakes as revealed by Cassini Huygens:

The RADAR instrument aboard Cassini detected dark regions that have been interpreted as liquid filled surfaces. The smooth surface of these regions acts as a mirror reflecting the transmitted signal away from the RADAR detector [1].

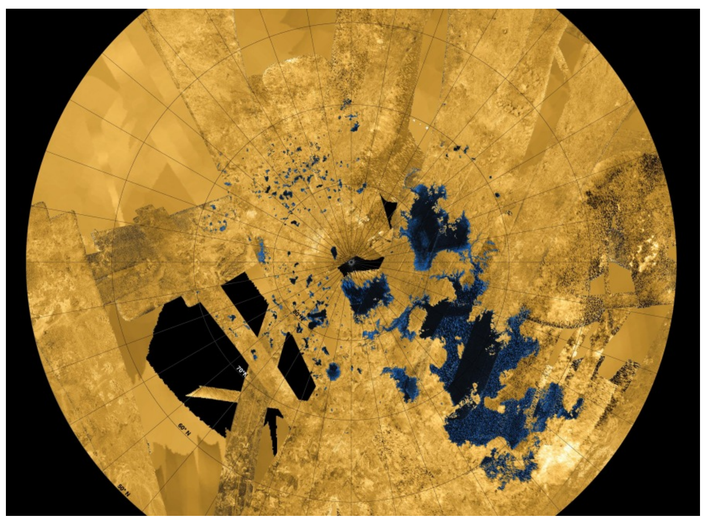

Image credit: Radar Mapper, JPL, USGS, ESA, NASA

- Most of the lakes are located in the northern hemisphere. Ontario lacus is the only lake near the southern pole
- VIMS detected ethane in correlation with Ontario Lacus lake [2].
- The detection of Methane is very difficult due to the strong absorption bands of gaseous CH_4 existing in the atmosphere and the similarity between infrared spectra of liquid and gaseous Methane.
- Recent *Cassini* Radar observations revealed an echo from the lake's bottom [3]. A low dielectric attenuation factor is needed within the lakes to explain these data< lakes are in fact dominated by methane ?

What we know about the chemical composition of Titan's lakes

Most studies aiming to determine the composition of Titan's lakes used theoretical modelling to determine this composition. Different theoretical approaches results in important discrepancies in the predicted hydrocarbon proportions in equilibrium between Titan's atmosphere and surface [4] [5].

	Cordier et al., 2009, 2013		Tan et al., 2013	
	Pole	Equator	Pole	Equator
N_2	5.91×10^{-3}	3.67×10^{-3}	2.20×10^{-1}	6.89×10^{-2}
CH_4	1.09×10^{-1}	6.34×10^{-2}	6.84×10^{-1}	3.17×10^{-1}
Ar	5.52×10^{-6}	3.52×10^{-6}	3.00×10^{-5}	1.12×10^{-5}
CO	5.10×10^{-7}	2.57×10^{-7}	2.12×10^{-5}	9.45×10^{-6}
C_2H_6	7.72×10^{-1}	8.14×10^{-1}	8.25×10^{-2}	5.31×10^{-1}
C_3H_8	7.49×10^{-2}	7.90×10^{-2}	7.80×10^{-3}	7.20×10^{-2}
C_4H_8	1.41×10^{-2}	1.48×10^{-2}		
H_2	3.92×10^{-6}	4.41×10^{-6}	1.73×10^{-6}	4.40×10^{-7}
HCN	1.17×10^{-5}	2.42×10^{-5}		
C_4H_{10}	1.23×10^{-2}	1.29×10^{-2}		
C_2H_2	1.16×10^{-2}	1.22×10^{-2}	3.40×10^{-3}	7.7×10^{-3}
C_6H_6	5.97×10^{-5}	1.10×10^{-4}		
CH_3CN	5.12×10^{-5}	9.90×10^{-5}		
CO_2	2.95×10^{-4}	3.11×10^{-4}		

- Based on the same atmospheric composition, different models obtain methane and ethane fractions that differ by one order of magnitude.
- There are big differences between the chemical composition of pole and equator lakes as calculated by Tan et al. 2013: CH_4 dominated lakes in the pole region and C_2H_6 dominated lakes in the equator region. The difference is less important in the Cordier et al. model.

➡ There is a need for experimental measurements to better constrain theoretical models.

Experimental setup: Titan's Lakes Simulation System (TiLSS)

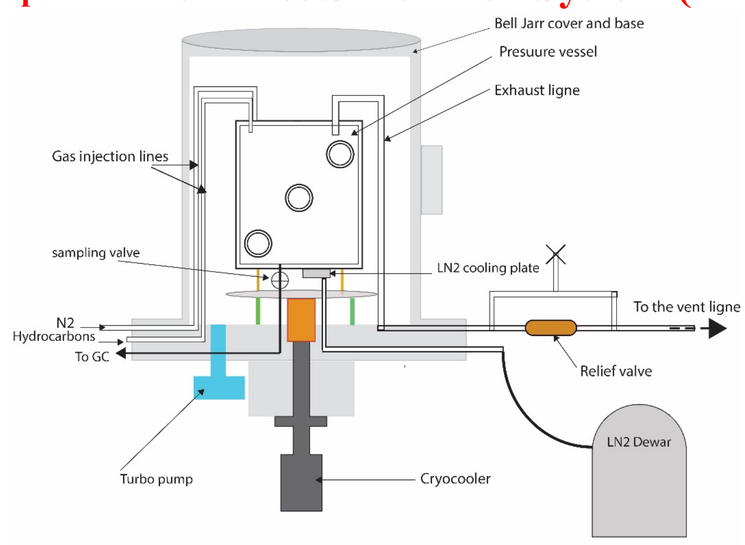

Diagram of the TiLSS setup

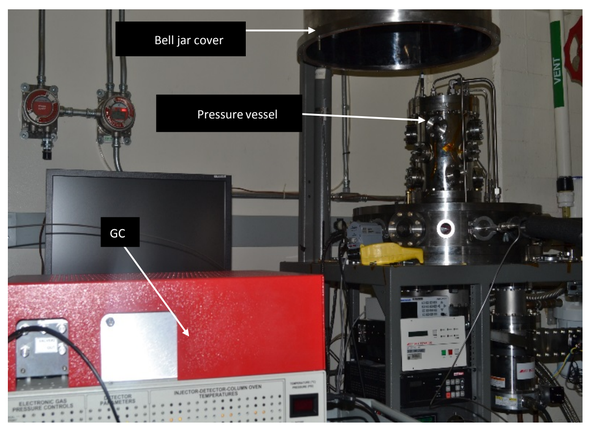

Photograph of the whole Titan's Lakes Simulation System (TiLSS), The pump and the head of the cryostat (not visible) are located below the cart

- Ability to measure the composition of liquid in equilibrium with a gas mixture (N_2, CH_4,C_2H_6, C_3H_8) mimicking the composition of Titan's atmosphere.
- The condensation environment reproduces the conditions on Titan's surface (T = 1.5 bar and T = 92 K) and liquid and vapor compositions are analyzed using a Gas Chromatograph.

Proof-of-concept performance test

- Test the ability of the system to reach T relevant to Titan: T can reach values as low as 80 K
- Test of the stability of temperature: 92 K ±0.01 in 48 hours
- First condensation test: The condensation of ethane at 150 K under 1.5 bar of N_2. The liquid sampled and analyzed by GC.
- Determination of molar fraction of dissolved nitrogen: 2.5 % of nitrogen dissolved at ethane, value consistent with Banitto et al. 1989 measurements at T = 150 k and P = 1 and 10 bar

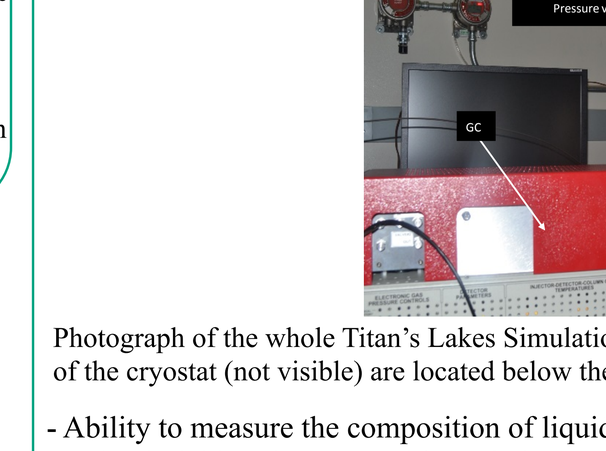

Good stability of T in the top and bottom of the condenser (T = 92 ±0.01 in 48 hours)

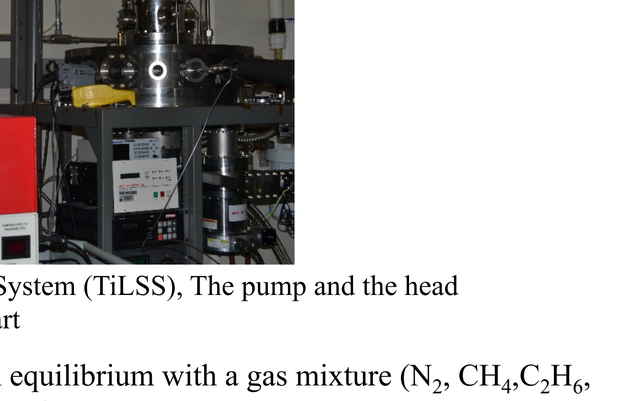

Gas chromatography spectrum of liquid ethane condensed at 150 K at 1.5 bar of nitrogen. The first peak at 1.63 min is assigned to nitrogen dissolved in ethane (peak 3.16 min)

References

[1] Stofan, E. R. et al.. Nature 445, 61–64, 2007.
[2] Brown, R. H. et al. Nature 454, 607–610, 2008.
[3] Mastrogiuseppe M. et al. GRL, 41,1432,2014.
[4] Cordier D., Mousis O., Lunine J. I., Lavvas P., Vuitton V. APJ, 707, 2009.
[5] Tan S. P., Kargel J.S., Marion G. M., Icarus, 222, 53-57, 2013.

Conclusion and impact :

An experimental setup has been designed and developed at JPL to synthesis Titan's lakes analogues. The main goal of this experimental platform is to better constrain theoretical modelling of chemical composition of Titan's lakes. The new setup will allow direct measurements of the chemical composition of lakes and its variation.

The research described here was carried out at the Jet Propulsion Laboratory, California Institute of Technology, under a contract with the National Aeronautics and Space Administration (NASA), and at the Division of Geological and Planetary Sciences at the California Institute of Technology.

Poster No. P 13

National Aeronautics and Space Administration

Kinetics of Methane Clathrate Formation in the Presolar Nebula

Author: Tuan H. Vu (3227)

Co-Author: Mathieu Choukroun (3227)

Introduction

- Clathrate hydrates, also known as "burning ice", are a type of inclusion compounds where small hydrocarbons such as methane and ethane are trapped inside symmetric cages of water ice.

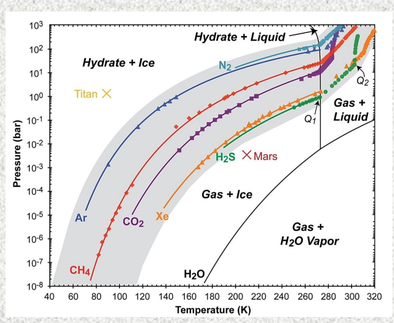

- Pressure/temperature conditions for formation and the structures of the cages depend largely on the size of the guest molecules.
- Clathrates have been suggested to be present on comets and a number of icy planetary bodies, including Mars, Europa, Titan, and Enceladus.
- This work focuses on the role of clathrate hydrates as a potential trap for volatiles during the presolar nebula.

Motivation

- Prior to *Voyager*, the prevailing expectation was that the elemental composition of the giant planets was reflective of the solar nebula composition and was therefore similar to solar abundances.
- However, spacecraft and ground-based observations have revealed unexpected elemental enrichment of C, N, S, As, P, and the noble gases in giant planets and comets.
- One of the leading explanations is the trapping of these volatiles species in clathrate hydrates.
- The goal of this work is to elucidate the clathrate formation kinetics under nebula-relevant conditions and determine whether clathrates could have formed and trapped the volatile species bearing these elements.

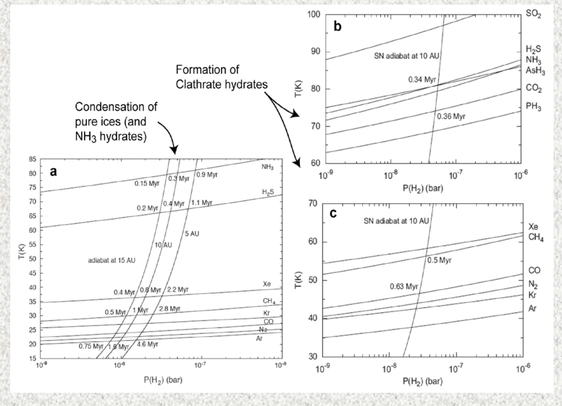

(a) Condensation curves of pure ices and adiabats of the solar nebula at 5, 10, 15 AU. (b) Stability curves of clathrates and (c) adiabat of the solar nebular at 10 AU. After Lunine et al. (2009) Titan from Cassini-Huygens; Springer, Chapter 3, 35-59

Experimental Setup

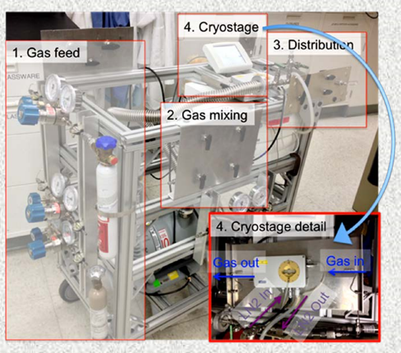

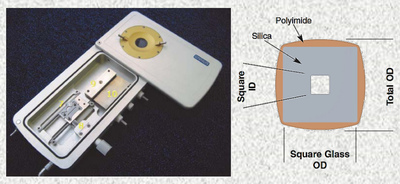

Photograph of the Linkam CAP 500 high-pressure cryostage. The capillary has a square cross-section and is guided to the optical area (#9) after locking (#7).

- A high pressure apparatus (up to 200 bars) was developed to study clathrate kinetics.
- Samples of methane clathrate are synthesized *in situ* at 223-253 K and 30-50 bars in a temperature-controlled Linkam CAP 500 cryostage.
- Kinetics of formation are monitored via changes in the microscopic images and in the Raman spectral features as a function of time until equilibrium is reached.

Kinetics of Formation

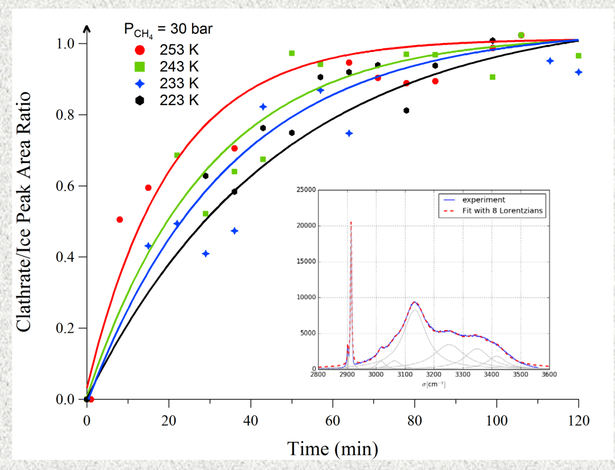

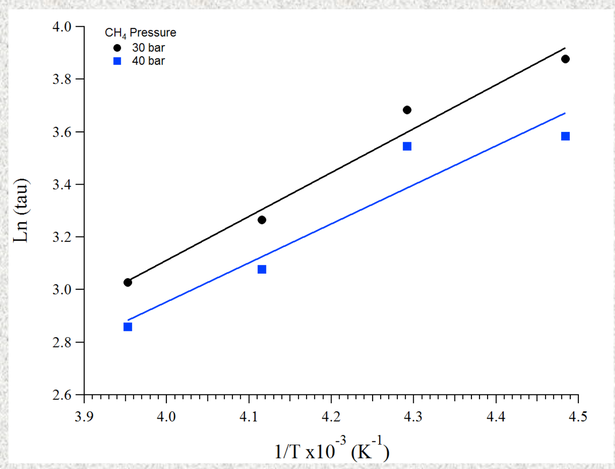

- Clathrate formation was observed within minutes upon pressurization of ice particles with 30-50 bars of gaseous methane.
- Experimental Raman spectra are deconvoluted into eight Lorentzian lines (top figure, inset). Growth is monitored by the ratio of peak areas between the clathrate peak at 2903 cm^{-1} and the sum of all the ice peaks from 3100 to 3500 cm^{-1}.
- Results show that clathrate growth proceeds faster at warmer temperatures and higher pressures.
- Bottom figure shows an Arrhenius plot of ln(τ), the characteristic time constant for clathrate formation, versus 1/T. This produces a linear fit with slope E_a/R, where E_a is the activation energy and R is the gas constant.
- Activation energies of 12.3 kJ/mol and 13.9 kJ/mol are obtained for methane clathrate formation at 40 bar 30 bar CH_4 pressures, respectively. These results indicate that the energy barrier for clathrate formation is rather low, with gas diffusion the likely limiting factor.

Micro-Raman Observation

Methane Clathrate Formation at 40 Bar

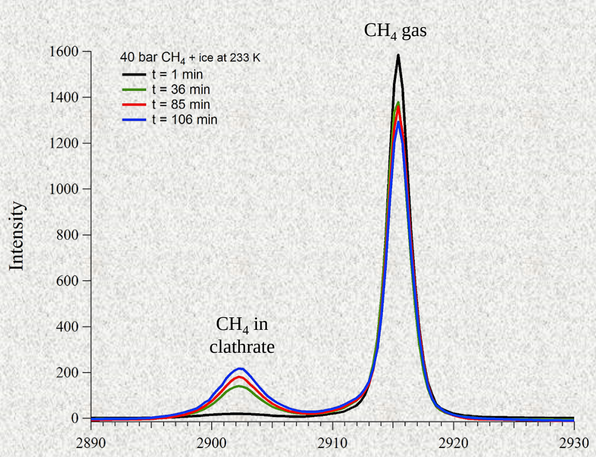

Raman spectra (left) show evolution of the 2903 cm^{-1} peak, characteristic of the υ_1 symmetric stretch of enclathrated CH_4, over time. Note the morphological change in the ice textures in the corresponding microscope images.

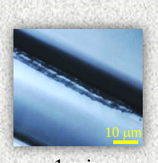

1 min

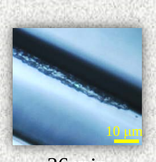

36 min

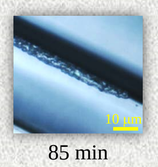

85 min

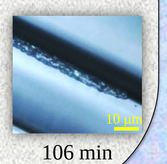

106 min

Conclusions

- High-pressure experiments have been conducted to measure the kinetics of methane clathrate formation, bringing forth new information on the timescales that would be required for this process to occur under nebula conditions.
- Results suggest that, for small ice particles on the order of ~50 μm, methane clathrate formation occurs on a rather fast timescale, with activation energies similar to those for diffusion of gas through water ice.
- Subsequent work will extend to other types of clathrates (H_2S, N_2) in order to fully evaluate the contribution of clathrates in the trapping of volatiles during the pre-solar nebula.

National Aeronautics and Space Administration

Jet Propulsion Laboratory
California Institute of Technology
Pasadena, California

www.nasa.gov

Acknowledgements

This work was conducted at the Jet Propulsion Laboratory, California Institute of Technology, under contract with NASA. Support from the NASA Origins of Solar Systems Program and government sponsorship are gratefully acknowledged.

Poster No. P-14

National Aeronautics and Space Administration

Photochemistry of condensed species on Titan‘s aerosols analogues

Benjamin Fleury (3227)
Murthy Gudipati (3227)

Introduction

Titan’s aerosols formation is initiated in the upper atmospheric layers at about 1000 km by the dissociation and the ionization of N_2 and CH_4 by the VUV solar photons [1]. Then, they aggregate and sediment to the surface. The temperatures of the stratosphere and the troposphere (measured by the HASI instrument onboard the Huygens probe [2]) allow the condensation of many volatile organics on the solid aerosols, forming organic ice coating on the aerosol polymers [3]. If high-energy solar photons initiating the organic chemistry in the ionosphere of Titan’s have been significantly absorbed at the altitude where species can condense, photons with longer wavelengths (λ > 300 nm) are still present at altitude as low as 100 km and could drive photochemistry of condensed species on aerosols, similar to photochemistry of condensed ices at these wavelengths demonstrated recently in the laboratory [4].

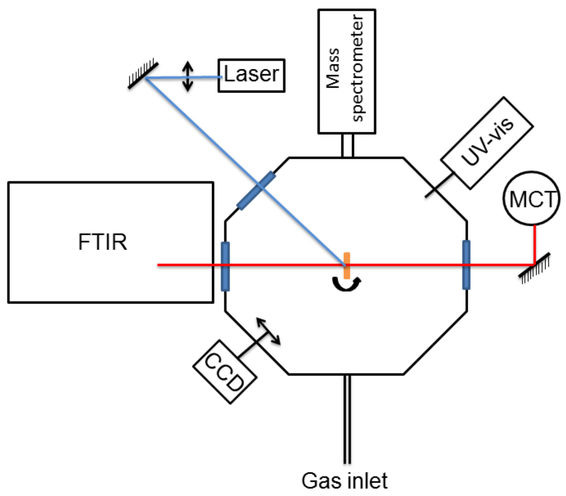

Figure 1: Scheme of the experimental setup at the JPL’s Titan Organic Aerosol Spectroscopy and chemisTry (TOAST) laboratory.

Laboratory simulation

To study this phenomenon, we irradiate condensed species coated on a blank sapphire window or on thin films of Titan’s aerosols analogues, names tholins, with a laser at 355 nm. The aerosols analogues are produced by subjecting a N_2-CH_4 gaseous mixture to a radio-frequency discharge [5]. A blank sapphire window or a tholins sample is mounted in the experiment presented in Figure 1. C_2H_2 is deposited at 50 K to form an ice film on the top of the tholins sample. C_2H_2 is one of the most abundant species in the atmosphere of Titan’s with a mixing ratio about 2 ppm_v as measured by the CIRS instrument at 120 km [6].

Mass spectrometry monitoring of the C_2H_2 desorption

The evolution of the signal at the *m/z* 26 (C_2H_2) during the irradiation of C_2H_2 coated on tholins is monitored using mass spectrometry.

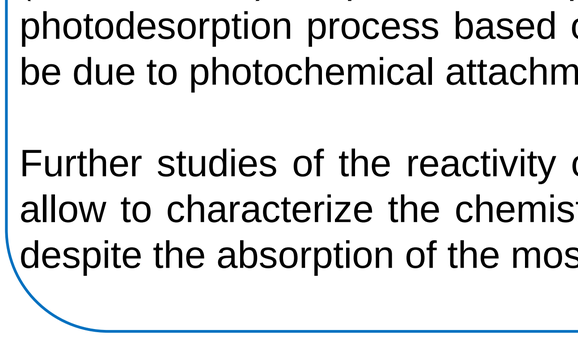

Figure 4: Evolution of the *m/z* 26 signal in the experiment as a function of the time during the C_2H_2 irradiation.

Figure 4 showed an increase of the signal at *m/z* 26 during the irradiation. Photodesorption of C_2H_2 occurred during the irradiation, explaining a part of the acetylene consumption measured by IR spectroscopy.

IR monitoring of the C_2H_2 consumption

The consumption of C_2H_2 after the irradiation is measured with IR spectroscopy by monitoring the evolution of the C-H absorption band of C_2H_2 at 3225 cm^{-1}.

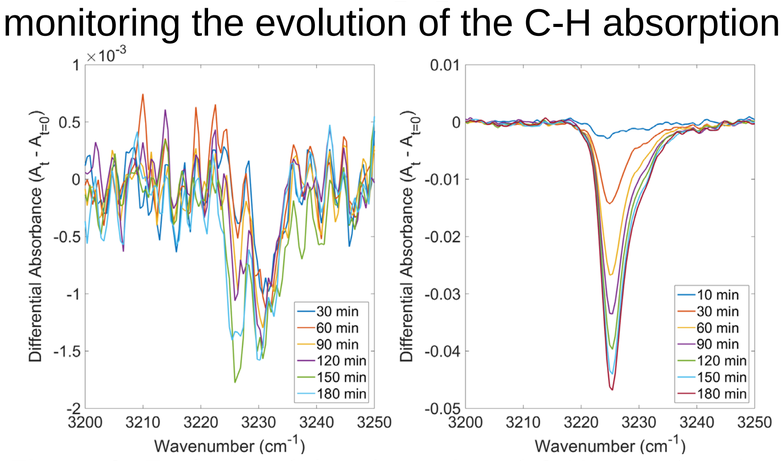

Figure 2: Evolution of the absorption of C_2H_2 as a function of the irradiation time when condensed on a blank sapphire window (left) or on a tholins sample (right).

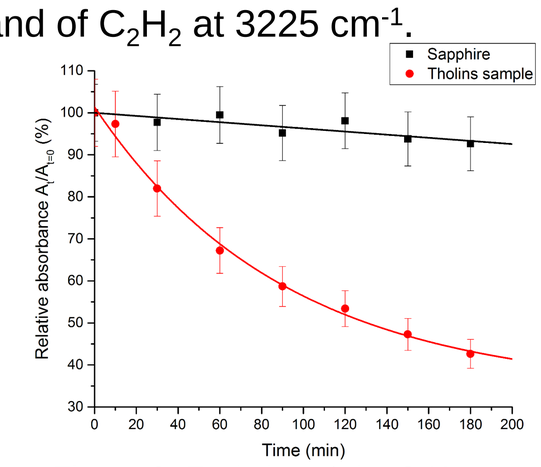

Figure 3: Evolution of the C_2H_2 amount as a function of the irradiation time.

Figure 2 and 3 showed that a higher consumption of C_2H_2 coated on a tholins sample occurred when compared to the irradiation of C_2H_2 ice film alone. This demonstrates that organic aerosols drive the photoreactivity of C_2H_2 when they are irradiated by long wavelength photons (355 nm).

Conclusion and Perspectives

We demonstrated experimentally that analogues of organic aerosols covering Titan’s surface drive the photodepletion of condensed species such as acetylene when they are irradiated with long wavelength photons (λ > 300 nm). A part of this photodepletion can be explained by a photodesorption process based on mass spectrometry while rest should be due to photochemical attachment of acetylene to the tholin polymer.

Further studies of the reactivity of other molecules present on Titan will allow to characterize the chemistry, which could occurr on Titan surface despite the absorption of the most energetic photons by the atmosphere.

References

[1] Waite, J. H., et al., The process of Tholin formation in Titan’s upper atmosphere, (2007), Science 316, 870-875.
[2] Fulchignoni, M., et al., In situ measurements of the physical characteristics of Titan’s environment, (2005), Nature 438, 785-791
[3] Lavvas, P., et al., Condensation in Titan’s atmosphere at the Huygens landing site, (2011), Icarus 215, 732-750.
[4] Gudipati, M. S. et al., Photochemical activity of Titan’s low-altitude condensed haze, (2013), Nature Communications 4, 1648.
[5] Szopa, C., et al., PAMPRE: A dusty plasma experiment for Titan’s tholins production and study, (2006), planetary and Space Science, 54, 394-404.
[6] Vinatier, S., et al., Vertical abundance profiles of hydrocarbons in titan’s atmosphere at 15° S and 80° N retrieved from Cassini/CIRS spectra, (2007), Icarus, 188, 120-138.

Acknowledgments

This work is supported by NASA Solar System Workings grant " Photochemistry in Titan’s Lower Atmosphere". The research work has been carried out at the Jet Propulsion Laboratory, California Institute of Technology under a contract with the National Aeronautics and Space Administration.

National Aeronautics and Space Administration
Jet Propulsion Laboratory
California Institute of Technology
Pasadena, California

www.nasa.gov

Poster No. P-15

National Aeronautics and Space Administration

Asteroid Gravity Fields – when 2 + 2 ≠ 4

Author: Simon Tardivel (312)
Advisor: Andrew T. Klesh (312)

What is the problem?

- Asteroids and comets come in many shapes and sizes:
  weird shapes = weird mass distributions = weird gravity fields
- The homogeneous polyhedron model is a great model for computing the gravity field/force… but the computation takes a lot of time! (linear complexity)
- The idea: why not pack a lot of spheres ("mascons") inside the polyhedron?
  ➔ computing gravity of many spheres could be much faster!
- **Can we accurately and efficiently model the gravity field of a homogeneous polyhedron with many homogeneous spheres?**

Mascons in polyhedrons

- What are mascons? "mass concentrations"
  - they are homogeneous spheres
  - their parameters are radius and density
- What should a good mascon packing be like?
  - are large internal gaps ok?
  - can mascons extend above the surface?
  - are overlapping of mascons ok?
  - are different radii/densities ok?

For faster computations, we restricted the mascons to a primitive cubic grid.

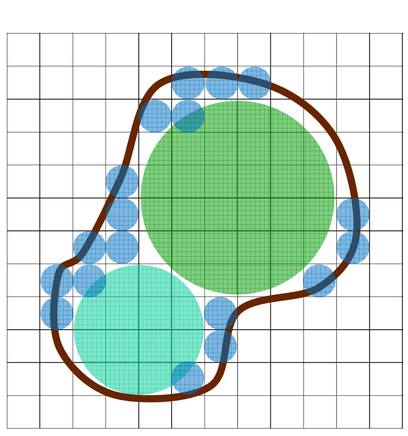

What do you think of this packing?
Would you do things differently?

Different packing methods

How would you pack mascons within a polyhedron?

1999 KW4 Alpha

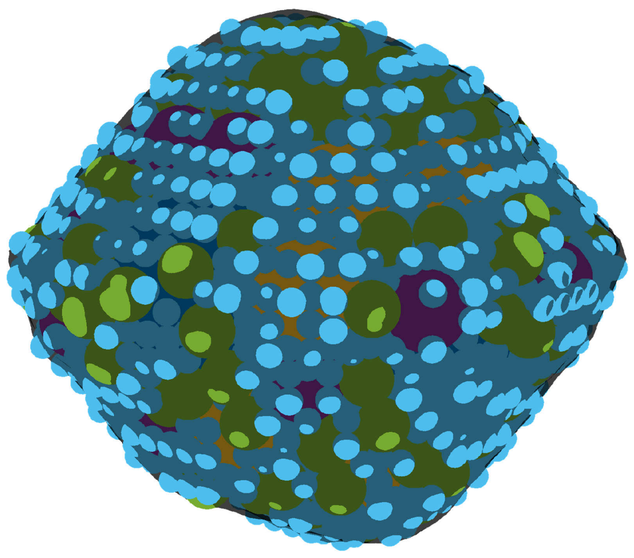

Itokawa

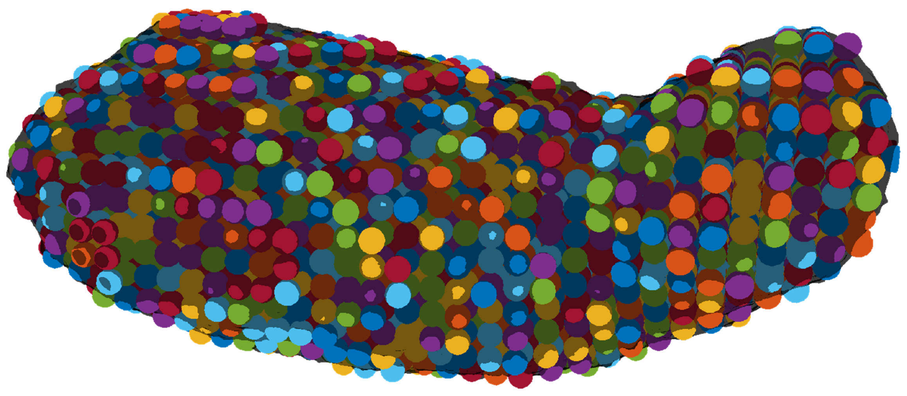

2008 EV5

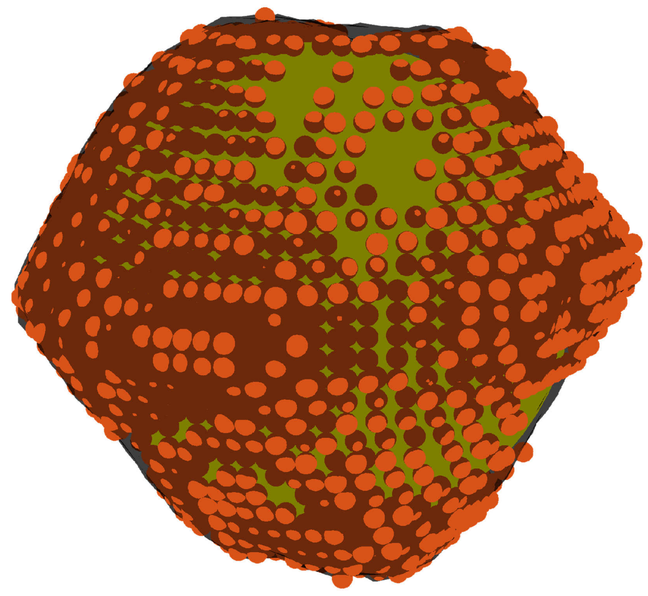

Method "Gumballs"
- Use mascons of different radii
- Pack in decreasing order of mascons radii

Porosity of the aggregate ≈ 20-30%

NB: it is recommended to limit the size of the largest mascons to avoid larger variations of bulk density within the body. It is also possible to slightly lower mascon densities with their radius

Method "Jellybeans"
- Fill every cube of the grid with a small mascon
- … that's it…

Porosity of the aggregate ≈ 47.64% (cP crystal)

NB: it is possible to do the same computation for 4 interlocking grids, to form a cF crystal. The spheres should be slightly smaller ($\sqrt{2}/2$), and it reduces porosity to its minimum value for identical spheres packing (≈26%)

Method "Sprinkles"
- First, place the largest mascon possible
- Then, use "jellybeans" to fill the gaps

Porosity of the aggregate ≈ 10-30%

NB: you must adjust (lower) the density of largest mascon! Without this step, the model would have a core with a much higher bulk density, hence terrible accuracy

What are the results?

- Mascons can be fast and accurate enough in some cases, or with enough of them
- But mascons are not a miracle solution:
  - a large number of mascons is required at least 100,000 for decent accuracy!
  - other models can be better and faster (situation specific)
- The computational speed gain has limits:
  - 1,000 facets ≈ 100,000 mascons
  - Shapes from radar have between 300 and 10,000 facets.
- **A low-resolution polyhedron model is faster than its mascon equivalent**

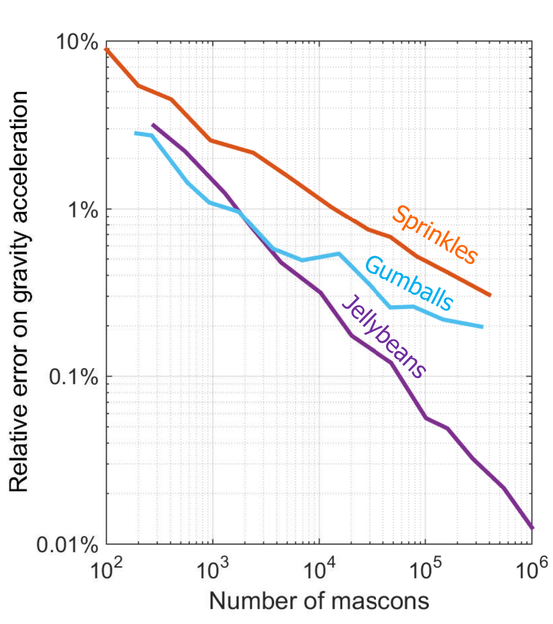

Different methods, different accuracies
E.g. 2008 EV5, at ≈0.25 R altitude

The bigger picture: local inhomogeneity

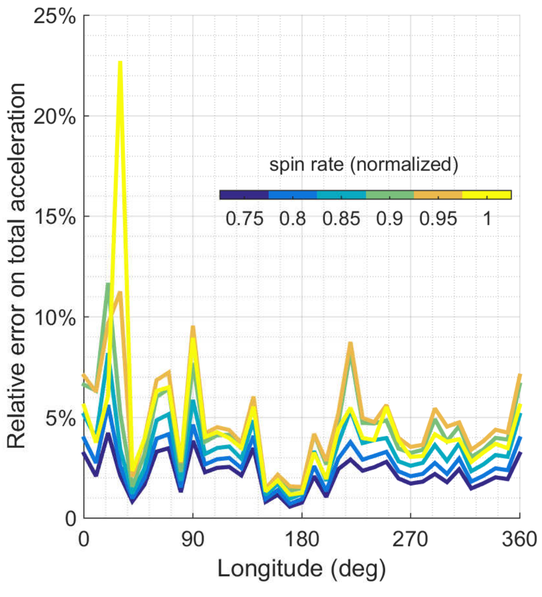

0.1-1% error on gravity means 5-25% acceleration error at the surface equator

- Spin a body fast enough and gravity and centrifugal acceleration balance at the equator. Then, any error on gravity estimation is magnified when estimating the total acceleration felt, close to the surface
- **But asteroids are neither mascons nor homogeneous polyhedron…
  they are, at least, a bit of both!**

➔ **Local inhomogeneity could mean 10% error on surface dynamics estimation**

➔ **Local inhomogeneity could have massive effects on internal structure**

National Aeronautics and Space Administration

Jet Propulsion Laboratory
California Institute of Technology
Pasadena, California

www.nasa.gov

Poster No. P-16

The Colors of Irradiated Mixed Ices and Application to Kuiper Belt and Jupiter Trojan Small Bodies

Michael J Poston (Caltech – 389K)
Jordana Blacksberg (389K), Mike Brown (Caltech), Robert Carlson (3227), Bethany Ehlmann (3220-Caltech), John Eiler (Caltech), Kevin Hand (3220), Robert Hodyss (3227), Ahmed Mahjoub (3227), and Ian Wong (Caltech)

Introduction / Problem

Dynamical models (REFS!) suggest that Kuiper Belt Objects (KBOs) and Jupiter Trojan asteroids have a common origin. This is supported observationally by a similar biomodal distribution of visible/near infrared (VNIR) spectral slopes for small bodies in each population. The two spectral groups are dynamically indistinct within each population, ruling out many possible histories. However, the slopes, albedos, and population statistics are not identical between KBOs and Trojans. Our project is a multi-pronged effort to better understand these bodies and the implications for the history of the solar system.

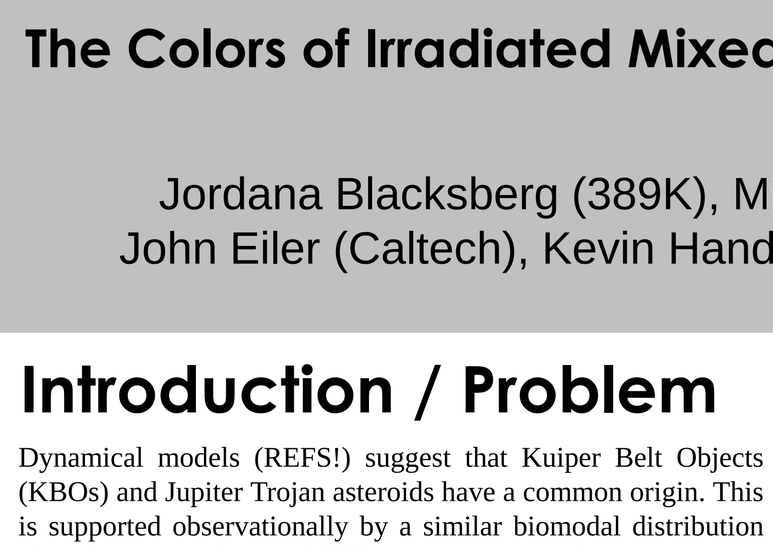

This figure demonstrates the bimodal population of small (>12.3 H magnitude) Jupiter Trojan asteroids. Main figure is taken from Wong, Brown, and Emery (*AJ* 2014). Inset (taken from Emery et al. (*AJ* 2011)) is the averaged spectra corresponding to the blue and red data in the main figure. Orange box highlights the spectral region analyzed in our experiments.

This poster focuses on laboratory simulations of a hypothesized history of these bodies (Wong and Brown, *AJ*, submitted). According to our hypothesis, the two spectral groups are the result of space weathering of objects with different surface compositions. All objects formed spanning the H_2S sublimation line; those formed outside the line contained H_2S at the surface while those formed inside did not. Irradiation formed a refractory "space weathered" crust, with the inclusion of sulfur leading to steeper VNIR slopes. After emplacement at their present-day locations the surfaces evolved the observed spectral differences. This hypothesis is shown schematically in the cartoon below.

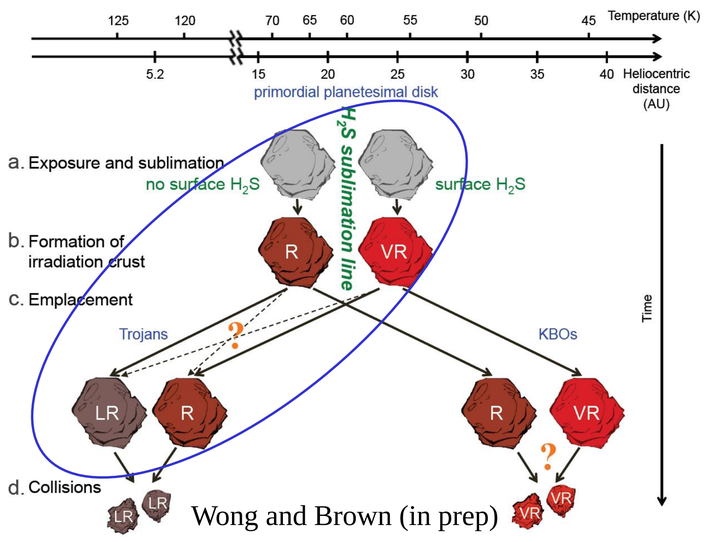

Wong and Brown (in prep)

Our team is made up of telescopic observers, modelers, laboratory chemists, and instrument developers, all working together toward the goal of understanding the physics and chemistry behind the observations. Among our goals is identifying diagnostic chemicals. Identification of such chemicals will influence mission and payload design for New Frontiers-class mission proposals to Trojan asteroids.

National Aeronautics and Space Administration
Jet Propulsion Laboratory
California Institute of Technology
Pasadena, California

www.nasa.gov

This work has been supported by the Keck Institute for Space Studies (KISS). The research described here was carried out at the Jet Propulsion Laboratory, Caltech, under a contract with the National Aeronautics and Space Administration (NASA) and at the Caltech Division of Geological and Planetary Sciences.

Poster No. P-18

Methodology

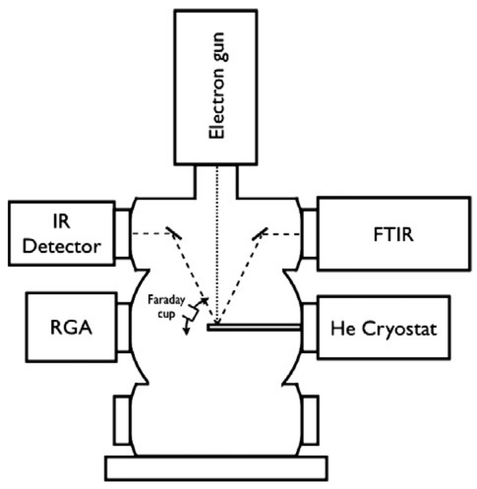

The reaction system is a stainless steel high vacuum chamber (lowest observed pressure about 6 x10^{-9} torr) equipped with a quadrupole mass spectrometer (RGA), closed-cycle He cryostat, electron gun and Faraday cup, gas dosing manifold, and windows and mirrors for a Fourier Transform Infrared (FTIR) spectrometer and a Visible/Near Infrared (Vis/NIR) Spectrometer (not pictured). The ice is vapor deposited on a gold mirror on the coldfinger. Irradiation is by 10 keV electrons at 500 nanoAmps.

Deposition (50 K) → Irradiation (50 K) 10 keV e^- beam → Heating to 120 K at 0.3 K/min with irradiation → Hold at 120 K

Results

Selected spectra from the methanol-ice irradiation at 50K are shown at right. Methanol-ice was analyzed primarily to directly test how the present experiment compared to previous work by other investigators under similar conditions.

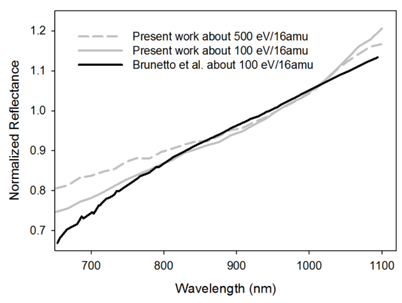

Gas Mixture Composition		Thickness (μm)		Irradiation (hr)		Total dose (eV/16 amu)	
Gases	**Ratio**		**+/-**	**at 50K**	**at 120K**	**at 50K**	**at 120K**
CH_3OH	pure	10	3	18	4	500	100
Round 1: Specular							
$H_2O : CH_3OH : NH_3$	1:2:2	30	10	24	23	700	700
$H_2O : CH_3OH : NH_3 : H_2S$	1:3:3:3	30	10	26	25	800	700
Round 2: Specular							
$H_2O : CH_3OH : NH_3$	1:2:2	40	10	24	29	700	900
$H_2O : CH_3OH : NH_3 : H_2S$	1:3:3:3	220	80	170	260	5000	8000
Round 3: Non-Specular							
$H_2O : CH_3OH : NH_3$	1:2:2	8	3	71	73	2000	2000
$H_2O : CH_3OH : NH_3 : H_2S$	1:3:3:3	60	20	77	69	2000	2000

Key parameters of each experiment. Radiation dose assumes a 1 μm irradiated layer and density equivalent to that of methanol.

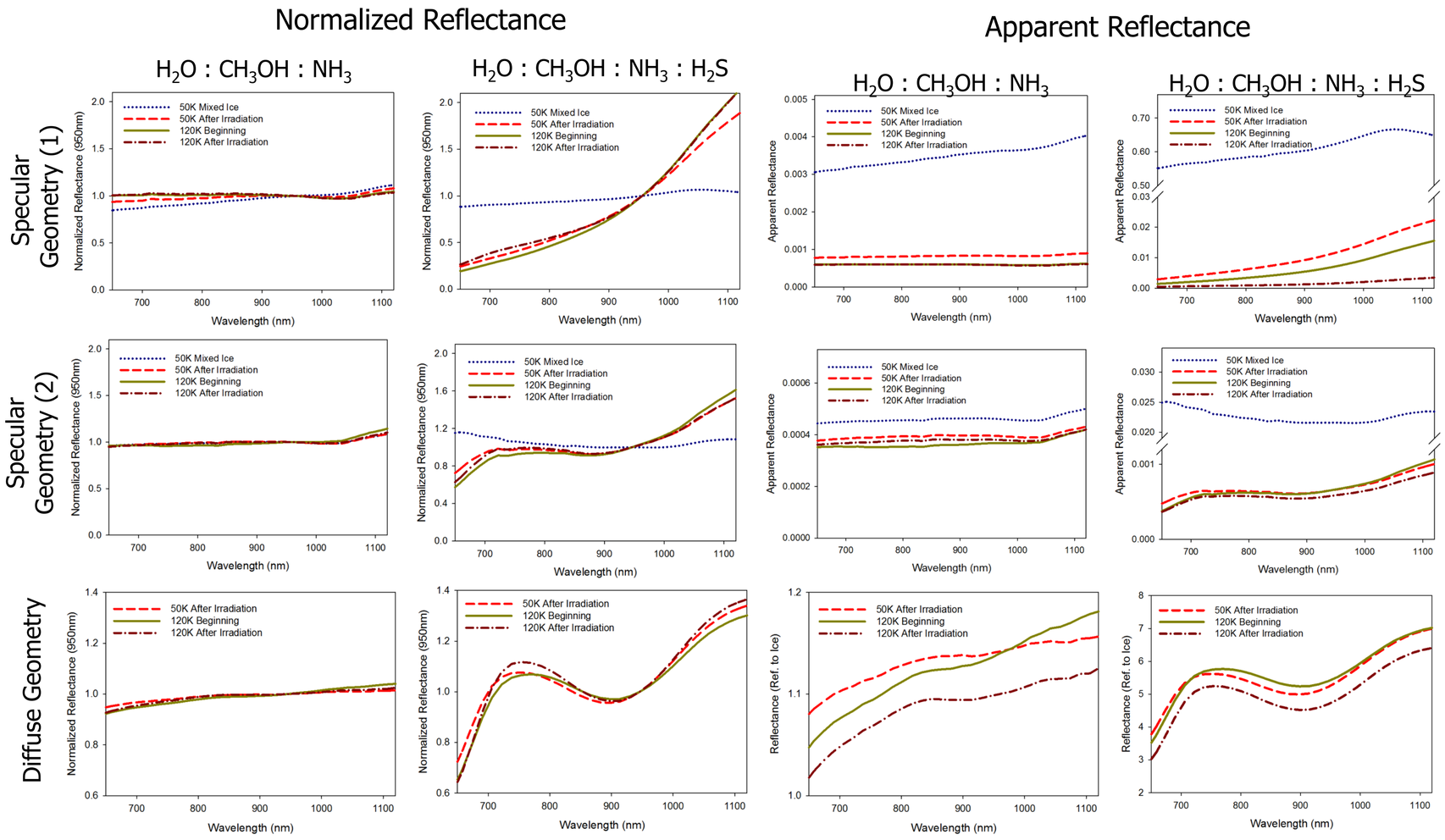

Gas Mixture Composition		Normalized Slope ($x10^{-4}$)				Relative Reflectance			
Gases	**Ratio**	**Ice**	**50K end**	**120K start**	**120K end**	**Ice**	**50K end**	**120K start**	**120K end**
CH_3OH	pure	--	7.8	--	--	--	--	--	--
Round 1: Specular									
$H_2O : CH_3OH : NH_3$	1:2:2	5.3	2.2	4.5	-0.3	$4x10^{-3}$	$8x10^{-4}$	$6x10^{-4}$	$6x10^{-4}$
$H_2O : CH_3OH : NH_3 : H_2S$	1:3:3:3	3.9	35	40	37	$6x10^{-1}$	$1x10^{-2}$	$7x10^{-3}$	$2x10^{-3}$
Round 2: Specular									
$H_2O : CH_3OH : NH_3$	1:2:2	1.6	1.6	2.9	2.0	$5x10^{-4}$	$4x10^{-4}$	$4x10^{-4}$	$4x10^{-4}$
$H_2O : CH_3OH : NH_3 : H_2S$	1:3:3:3	-1.6	12	16	13	$2x10^{-2}$	$7x10^{-4}$	$7x10^{-4}$	$6x10^{-4}$
Round 3: Non-Specular									
$H_2O : CH_3OH : NH_3$	1:2:2	0	1.2	2.3	1.7	1.0	1.12	1.13	1.09
$H_2O : CH_3OH : NH_3 : H_2S$	1:3:3:3	0	8.7	8.9	9.6	1.0	5.5	5.6	5.0

Key results are show in in the table at left.
Complimentary geometries were used to understand which spectral changes appear to be changes in scattering and which appear to be changes in absorbance. Changes due to varying the initial ice thickness appear to be dominated by changes in scattering properties of the ice. The correlated behavior of the slopes upon irradiation with electrons indicates absorption dominates the net behavior. Heating to 120K had similar effects on all samples: increased steepness of slope while relative reflectance remained about the same. Irradiation at 120K tended to decrease the spectral slope while total signal decreased slightly as well.

Interpretations / Conclusions / Impact

For the present experiment to strongly support our hypothesis the following three trends should exist:

1) Normalized spectral slopes should be steeper in the irradiated "with S" mixed ice.
2) Irradiated films should become less bright upon heating to 120K and further irradiation.
3) Normalized spectral slopes should flatten upon heating from 50K to 120K and further irradiation.

The present experiments strongly support trends (1) and (2). Trend (3) was weakly supported by the round 1 experiments, but was contradicted in the round 2 and 3 experiments with thicker ice films and longer irradiation times, rendering this portion of the experiment inconclusive. Therefore, while our results generally support the hypothesis, they do not support the simplest explanation – mixed ice irradiation products alone – for the potential relationship between Trojan and KBO spectra. However, the data are consistent with KBO spectra being dominated by ice irradiation products and Trojan spectra being a mix of ice irradiation products and a more neutral material.

National Aeronautics and Space Administration

Large Synoptic Survey Telescope: Projected Near-Earth Object Discovery Performance

Peter Vereš (392R)
Steve Chesley (392R)

WILL LSST DISCOVER NEO? YES, IT WILL:

- 60±1% NEO with size>140m with automated linking at 100% efficiency
- 55±1% NEO with size>140m current automated linking efficiency
- Survey with 2-visits of the field per night WORKS for NEO discovery
- Fraction of all false orbits is only 0.5% after the automated linking

WHY IS THIS IMPORTANT?

- NASA Congressional Mandate to discover 90% NEO larger than 140m before 2020 (currently behind schedule)
- Planetary Defense & Space Resources
- Asteroid Redirect Mission (ARM)
- Crewed mission to asteroids

INTRODUCTION

LSST is a next generation optical survey telescope:

- Currently being built at El Peñón, Chile
- 8.4-m primary mirror
- Main mission 2022-2032 (first light 2020)
- Science: dark energy, gravitational lensing, Milky Way, transients, Solar System objects

Tasks:

- Fraction of large Near-Earth Objects (NEO) discovered?
- Will the automated processing work and deliver orbits?
- How do the constraints affect detection efficiency of NEO?
- Fraction of false orbits?

METHODOLOGY

Pan-STARRS Moving Object Processing System (MOPS) generated ephemerides of synthetic orbits and linked detections into intra-night tracklets, inter-night tracks and derived orbits.

MOPS: Detections – Tracklets – Tracks – Orbit

- NEO simulation in low fidelity mode (3000 randomly selected NEO) in three 10-years surveys – baseline with 2-visit per night, three-visit and four-visit optimized cadences generated in OpSim.
- High-fidelity simulation with full-density population - NEO (800,000 orbits), Main-Belt asteroids (15 million orbits) and noise in a time frame 1 – 3 months and to demonstrate automated linking of tracks to orbits.

HIGH FIDELITY CONSTRAINTS

- Realistic shape, orientation of the field (FOV)
- Missing pixels (fill factor)
- Magnitude loss due to vignetting
- Signal-to-noise losses due to trailing
- Fading - definition of limiting magnitude
- Light curve variation due to rotating asteroids
- Colors of asteroids (S and C types)
- Astrometric and photometric uncertainties, errors
- False detections: shot noise, artifacts

RESULTS

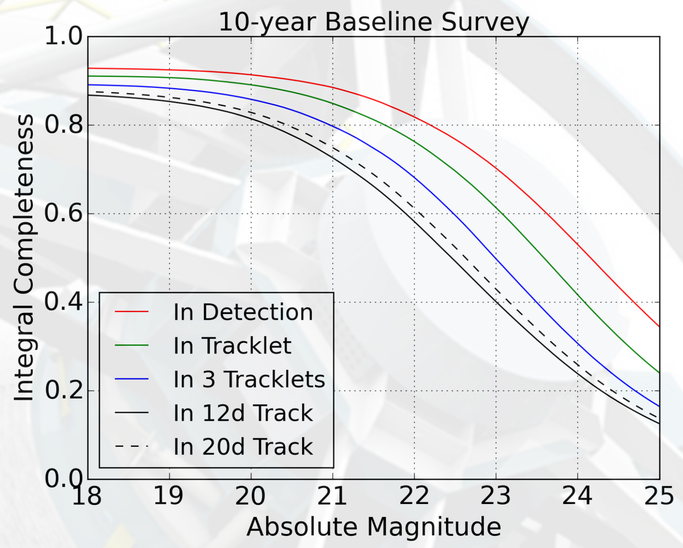

Baseline survey cadence is mostly optimized for 2 visits per night.

All constraints + 90% fill factor => 12 and 20 day tracks => ~ 60% completeness for H<22 corresponding to D<140m

What if 3 or 4 visits are required for the NEO discovery?

This will significantly decrease the integral completeness and make the NEO survey inefficient.

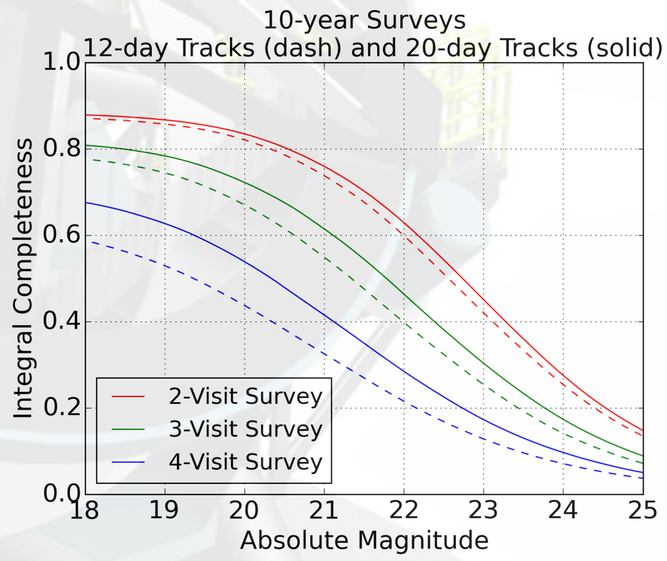

Sim ID	Obs. Cycle	NEO Model	MBAs Used	False Det. (Noise)	False Det. (Other)	linkTracklets Options vtree-thresh	pres_thresh	plate_width	NEO Eff. (All)	NEO Eff. (H<22)
A	3	Bottke	No	No	No	0.0030	0.0030	0.0010	98.9%	99.2%
B	1	Bottke	No	No	No	0.0030	0.0020	0.0001	97.0%	98.0%
C	3	Bottke	No	No	No	0.0010	0.0010	0.0010	70.0%	72.0%
D	1	Granvik	Grav	Yes	Yes	0.0004	0.0008	0.0001	70.0%	92.0%
E	1	Granvik	Grav	Yes	Yes	0.0010	0.0020	0.0100	70.0%	92.0%
F	1	Granvik	No	No	No	0.0020	0.0020	0.0030	90.6%	97.9%

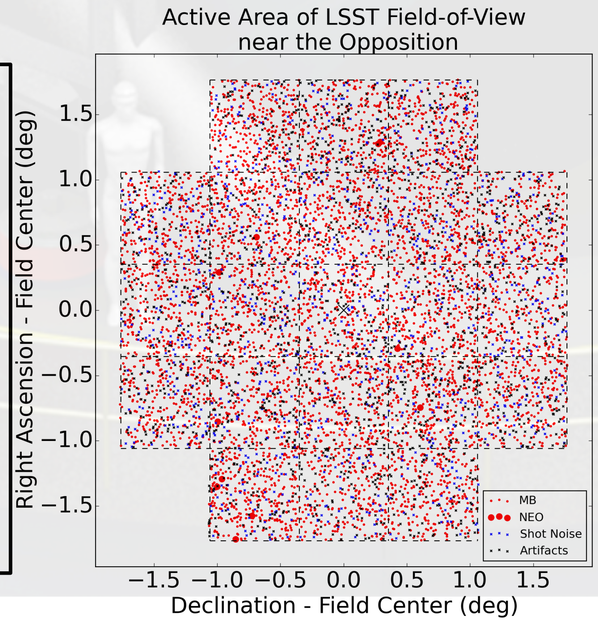

LINKING

Optimizing of automated linking to orbits by KD-tree search (table above) and multiple density models in 1 or 3 month observing cycles. Figure on the left shows the density of detections in a single field.

For large NEO, we achieved 92% linking efficiency.
Contamination of all orbits with false orbits is low (0.5%).
CPU, memory and orbit determination is still an issue that could be resolved by upcoming computing and cloud solutions.

National Aeronautics and Space Administration
Jet Propulsion Laboratory
California Institute of Technology
Pasadena, California

www.nasa.gov

Poster No. P-19